

Article

Centrality-Dependent Chemical Potentials of Light Hadrons and Quarks Based on p_T Spectrum and Particle Yield Ratio in Au-Au Collisions at RHIC Energies

Xing-Wei He ¹, Hua-Rong Wei ^{1,*}, Bi-Hai Hong ¹, Hong-Yu Wu ¹, Wei-Ting Zhu ¹ and Feng-Min Wu ²¹ Institute of Optoelectronic Technology, Lishui University, Lishui 323000, China² Department of Physics, Zhejiang Sci-Tech University, Hangzhou 310000, China

* Correspondence: huarongwei@lsu.edu.cn

Abstract: We analyze the p_T spectra of π^\pm , K^\pm , p , and \bar{p} produced in different centralities' Au-Au collisions at different collision energies from 7.7 to 62.4 GeV using a two-component Erlang distribution in the framework of a multi-source thermal model. The fitting results are consistent with the experimental data, and the yield ratios of negative to positive particles are obtained from the normalization constants. Based on the yield ratios, the chemical potentials of light hadrons (π , K , and p) and quarks (u , d , and s) are extracted. This study shows that only the yield ratios of p decrease with the increase in centrality. The logarithms of these yield ratios in the same centrality show obvious linear dependence on $1/\sqrt{s_{NN}}$. The extracted chemical potentials (the absolute magnitude for π) of light hadrons and quarks decrease with the increase in energy. The curves of chemical potential vs. energy for all centralities derived from the linear fits of the logarithms of the yield ratio as a function of energy have their maximum (the absolute magnitude for π) at the same energy of 3.526 GeV, which is possibly the critical energy of phase transition from a liquid-like hadron state to a gas-like quark state in the collision system.

Keywords: transverse momentum spectra; yield ratio of negative to positive particles; chemical potential of particle; critical end point of phase transition



Citation: He, X.-W.; Wei, H.-R.; Hong, B.-H.; Wu, H.-Y.; Zhu, W.-T.; Wu, F.-M. Centrality-Dependent Chemical Potentials of Light Hadrons and Quarks Based on p_T Spectrum and Particle Yield Ratio in Au-Au Collisions at RHIC Energies. *Universe* **2022**, *8*, 420. <https://doi.org/10.3390/universe8080420>

Academic Editors: Khusniddin Olimov, Fu-Hu Liu and Kosim Olimov

Received: 30 June 2022

Accepted: 11 August 2022

Published: 12 August 2022

Publisher's Note: MDPI stays neutral with regard to jurisdictional claims in published maps and institutional affiliations.



Copyright: © 2022 by the authors. Licensee MDPI, Basel, Switzerland. This article is an open access article distributed under the terms and conditions of the Creative Commons Attribution (CC BY) license (<https://creativecommons.org/licenses/by/4.0/>).

1. Introduction

The successful running of the Relativistic Heavy Ion Collider (RHIC) in 2000 and the Large Hadron Collider (LHC) in 2008 [1] attracted great interest in studying the evolution process of interacting systems in high-energy collision. A large amount of evidence confirms that such a high-energy collision system produces an extremely high temperature and high density environment, which makes the collision system experience the phase transition process from the hadronic matter to quark–gluon plasma (QGP) [2–4], and produces strong coupling quark–gluon plasma (sQGP) [5–7]. By studying the chemical freeze-out temperature (T_{ch}) of the interacting system and the chemical potential (μ_B) of baryon in the phase diagram of quantum chromodynamics (QCD) [8,9], one can obtain the information about the phase transition from hadronic matter to QGP and the properties of QGP, such as the possible critical end point (CEP) of phase transition [10,11]. Thus, it is important to study the baryon chemical potential in the $\mu_B - T_{ch}$ plane. Meanwhile, the chemical potentials of other particles, such as light hadron and quark, are also important and interesting in researching the evolution of collision systems, the mechanism of particle production and even the property of QGP. The final-state particles produced in high-energy collisions are multifarious and show many statistical behaviors that contain some information about the collision process [12–15]. It is interesting to find some useful information from these regular behaviors. After the kinetic freeze-out, the transverse momentum (p_T) of particle no longer changes [16]. Thus, by analyzing the p_T distribution of final-state particles, one can obtain information about kinetic freeze-out, even other stages of collision system. For

example, one can extract the kinetic freeze-out temperature of the interacting system, the flow velocity of particles and so on, directly from the p_T distribution [17]. One can also extract the yield ratio of negative to positive particles based on the p_T spectrum and the chemical potential of particles at the chemical freeze-out [18–21]. Meanwhile, one can also analyze the connections between these quantities and the collision size, energy, centrality, particle mass, and so on, then further extract a particle production mechanism and the information of other earlier stages.

Generally, one can use phenomenological models to describe the p_T spectrum of final-state particles. These models can be divided into microcosmic kinetics models and thermal statistical models. A thermal statistical model focuses on studying the collective or global statistical behavior of final-state particles. There are many theoretical distribution models in the framework of a thermal statistical model, such as Boltzmann distribution [22], blast-wave model [23], power-law function [24], Lévy distribution [25], Erlang distribution [17,26,27] and so on. In the framework of a multi-source thermal model [27–29], one can use the multi-component distribution model to improve the fitting degree of single-component distribution in the high p_T region. Meanwhile, more information can be extracted. For example, by using multi-component Erlang distribution, one can not only extract the relative yield of particles, but also the weight of hard (soft) excitation degree.

From the yield ratio of negative to positive particles, one can obtain the chemical potentials of hadrons and quarks at chemical freeze-out, according to reference [30]. While the yield ratio calculated from p_T spectrum of final-state particles, is actually at kinetic freeze-out when the yield ratio is affected by the strong decay from high-mass resonances and the weak decay from heavy flavor hadrons [31]. In order to obtain the yield ratio at chemical freeze-out, the contributions of strong decay and weak decay need to be removed from the yield ratio calculated from the p_T spectra. While according to the references [21,32], the strong and weak decays actually have less effect on the above particle yield ratio from normalization constants, although they have a big impact on particle yield. As such, we can approximately extract the chemical potentials of hadrons and quarks by using the yield ratio from normalization constants instead of the yield ratio modified by removing the contributions of strong and weak decays.

In the present work, we describe the p_T spectra of π^\pm , K^\pm , p , and \bar{p} produced in different centralities' Au-Au collisions over a center-of-mass energy ($\sqrt{s_{NN}}$) ranging from 7.7 to 62.4 GeV [33,34] using a two-component Erlang distribution [17,26,27] in the framework of a multi-source thermal model [27–29]. The energy- and centrality-dependent yield ratios of negative to positive particles were obtained according to the extracted normalization constants. Meanwhile, the energy- and centrality-dependent chemical potentials of light hadrons (π , K , and p) and quarks (u , d , and s) are then extracted from the yield ratios.

2. The Model and Formulism

In the present work, we used a two-component Erlang distribution [26,27] to describe the p_T spectra of the final-state light flavor particles to obtain the normalization constants, and to extract the yield ratios. The two-component Erlang distribution is regarded as the contribution of the soft excitation process and the hard scattering process. The soft excitation process comes from the interactions among a few sea quarks and gluons and results in the low- p_T region distribution, and the hard scattering process originates from a harder head-on scattering between two valence quarks and results in the high- p_T distribution. The two-component distribution is in the framework of a multi-source thermal model [27–29], and the method is as follows.

The multi-source thermal model assumes that many emission sources are formed in high energy-collisions. Due to the existence of different interacting mechanisms in the collisions and different event samples in experiment measurements, these emission sources are classified into l groups. According to a thermodynamic system, the p_T of particles generated from one emission source obey an exponential distribution,

$$f_{ij}(p_{tij}) = \frac{1}{\langle p_{tij} \rangle} \exp \left[-\frac{p_{tij}}{\langle p_{tij} \rangle} \right], \tag{1}$$

where p_{tij} and $\langle p_{tij} \rangle$ are the p_T of particles from the i -th source in the j -th group and the mean value of p_{tij} , respectively. Assume that the mean p_T of particles from each source in the same group is the same. Then, all the sources in the j -th group meet the distribution of the folding result of exponential distribution

$$f_j(p_T) = \frac{p_T^{m_j-1}}{(m_j-1)! \langle p_{tij} \rangle^{m_j}} \exp \left[-\frac{p_T}{\langle p_{tij} \rangle} \right], \tag{2}$$

where m_j is the source number in the j -th group and p_T denotes the p_T of particles from m_j sources, i.e.,

$$p_T = \sum_{i=1}^{m_j} p_{tij}. \tag{3}$$

This is the normalized Erlang distribution, which can describe the p_T distribution of the particles from the sources in the same group because they have the same excitation degree and stay at a common local equilibrium state. The contribution of all emission sources in all groups can be expressed as

$$f(p_T) = \sum_{j=1}^l k_j f_j(p_T), \tag{4}$$

where k_j is the relative weight of the j -th group sources and meets the normalization $\sum_{j=1}^l k_j = 1$. This is the multi-component Erlang distribution, which can describe the final-state p_T distribution. Then, the two-component Erlang p_T distribution can be written as

$$f(p_T) = k_1 f_1(p_T) + (1 - k_1) f_2(p_T). \tag{5}$$

According to the two-component Erlang p_T distribution, we describe the p_T spectra of π^\pm , K^\pm , p and \bar{p} produced in Au-Au collisions at different energies for different centralities, and obtain the normalization constants corresponding to the above particles. The ratios of normalization constants of antiparticles, π^- , K^- , and \bar{p} , to particles, π^+ , K^+ , and p , are the yield ratios of negative to positive particles at kinetic freeze-out. Neglecting the little contribution of the strong and weak decays to the yield ratios, the ratios of normalization constants are approximately equal to the yield ratios of particles at chemical freeze-out. Due to the fact that the experimental data of some particles correspond to a narrow p_T range, the normalization constant extracted by describing the p_T spectra of particles with two-component Erlang distribution may be more precise than the yield published by the Collaborations.

Based on the above yield ratios, we calculated the chemical potentials of some light hadrons (π , K , and p) and light quarks (u , d , and s). According to the statistical arguments based on the chemical and thermal equilibrium within the thermal and statistical model [35], the three types of yield ratios, k_π , k_K , and k_p , in terms of the light hadron chemical potentials, μ_π , μ_K , and μ_p , of hadrons π , K , and p , are to be [19,35,36]

$$\begin{aligned} k_\pi &= \exp \left(-\frac{2\mu_\pi}{T_{ch}} \right), \\ k_K &= \exp \left(-\frac{2\mu_K}{T_{ch}} \right), \\ k_p &= \exp \left(-\frac{2\mu_p}{T_{ch}} \right), \end{aligned} \tag{6}$$

where T_{ch} is the chemical freeze-out temperature of the interacting system. Within the framework of a statistical thermal model of non-interacting gas particles with the assumption of standard Maxwell–Boltzmann statistics [2,3,37], T_{ch} can be empirically obtained by the following formula

$$T_{ch} = T_{lim} \frac{1}{1 + \exp[2.60 - \ln(\sqrt{s_{NN}})/0.45]}, \tag{7}$$

where T_{lim} is the ‘limiting’ temperature and can be empirically taken to have a value of 0.164 GeV, and $\sqrt{s_{NN}}$ is in the unit of GeV [37,38].

Based on Equation (6) and references [19,39,40] under the same value of chemical freeze-out temperature for π , K , and p , we can obtain the three types of yield ratios in terms of the three types of quark chemical potentials (μ_u , μ_d , and μ_s for u , d , and s quarks, respectively) to be

$$\begin{aligned} k_\pi &= \exp\left[-\frac{(\mu_u - \mu_d)}{T_{ch}}\right] / \exp\left[\frac{(\mu_u - \mu_d)}{T_{ch}}\right] = \exp\left[-\frac{2(\mu_u - \mu_d)}{T_{ch}}\right], \\ k_K &= \exp\left[-\frac{(\mu_u - \mu_s)}{T_{ch}}\right] / \exp\left[\frac{(\mu_u - \mu_s)}{T_{ch}}\right] = \exp\left[-\frac{2(\mu_u - \mu_s)}{T_{ch}}\right], \\ k_p &= \exp\left[-\frac{(2\mu_u + \mu_d)}{T_{ch}}\right] / \exp\left[\frac{(2\mu_u + \mu_d)}{T_{ch}}\right] = \exp\left[-\frac{2(2\mu_u + \mu_d)}{T_{ch}}\right]. \end{aligned} \tag{8}$$

According to Equations (6) and (8), the chemical potentials of the above hadrons and quarks in terms of yield ratios can be, respectively, expressed as

$$\begin{aligned} \mu_\pi &= -\frac{1}{2}T_{ch} \cdot \ln(k_\pi), \\ \mu_K &= -\frac{1}{2}T_{ch} \cdot \ln(k_K), \\ \mu_p &= -\frac{1}{2}T_{ch} \cdot \ln(k_p), \end{aligned} \tag{9}$$

and

$$\begin{aligned} \mu_u &= -\frac{1}{6}T_{ch} \cdot \ln(k_\pi \cdot k_p), \\ \mu_d &= -\frac{1}{6}T_{ch} \cdot \ln(k_\pi^{-2} \cdot k_p), \\ \mu_s &= -\frac{1}{6}T_{ch} \cdot \ln(k_\pi \cdot k_K^{-3} \cdot k_p). \end{aligned} \tag{10}$$

In the present work, we only calculate the chemical potentials of the light hadrons of π , K , and p , and light quarks of u , d , and s . For the hadrons containing c or b quark, considering the fact that there is a lack of experimental data for the p_T spectra which continuously vary with energy or centrality, we do not calculate the chemical potentials of c and b quarks, and the hadrons containing c or b quark. In addition, due to the lifetimes of the hadrons containing t quark being too short to measure, we also cannot obtain the chemical potentials of t quark, and the hadrons containing t quark.

The above method is different from the conventional Hadron resonance gas (HRG) model [8]. Both baryo-chemical potential (μ_B) and T_{ch} are contained in the grand-canonical partition function of the hadron resonance gas. μ_B and T_{ch} are obtained by fitting the experimental hadron yield, which is directly collected from the international collaborations, to HRG Model. However, information about T_{ch} cannot be obtained for the nonexistence of the temperature parameter in the two-component Erlang distribution which is mainly used to attract the accurate yield. With the aid of the empirical formula (Equation (7)) about T_{ch} , the chemical potential of light hadrons and quarks can be calculated in this work. As μ_p is a proxy of μ_B , a comparison between them will be discussed in the next section.

3. Results and Discussion

Figure 1 shows the p_T distributions of (a)(d) π^\pm , (b)(e) K^\pm , (c) p , and (f) \bar{p} produced in Au-Au collisions at $\sqrt{s_{NN}} = 7.7$ GeV in different centrality classes of 0–5%, 5–10%, 10–20%, 20–30%, 30–40%, 40–50%, 50–60%, 60–70%, and 70–80%. Similarly, the p_T spectra for the energies of 11.5, 19.6, 27, 39, and 62.4 GeV are presented in Figures 2–6, respectively. dN/dy on the axis denotes the rapidity density. The symbols represent the experimental data recorded by the STAR Collaboration in the mid-rapidity range of $|y| < 0.1$ [33,34]. The spectra for all centralities are scaled by suitable factors for clarity. The uncertainties are statistical and systematically added in quadrature. The curves are our results calculated using the two-component Erlang distribution. It should be mentioned that the data with different centralities at same collision energy show a similar trend. The best fit of data to the two-component Erlang distribution is obtained according to the combination of the minimum of χ^2 and the shape of the curves. However, in our previous work [21], only χ^2 was considered. The values of free parameters (m_1 , p_{ti1} , k_1 , m_2 , and p_{ti2}), normalization constant (N_0), and χ^2 per degree of freedom (χ^2/dof) corresponding to the two-component Erlang distribution for different energies are, respectively, listed in Tables 1–6, where the normalization constant is for comparison between curve and data. One can see that the two-component Erlang distribution can well describe the experimental data of the considered particles in Au-Au collisions at all energies for all centrality classes. The tables show that the values of m_1 correspond to a low- p_T region for all particles at all energies in all centrality classes are 2, 3, or 4, and all m_2 corresponding to high- p_T region are 2, which shows that the soft process originates from the interaction among 2, 3, or 4 sea quarks and gluons, and the hard process originates from a hard head-on scattering between two valence quarks. The values of the relative weight factor k_1 of the soft excitation process are more than 60%, which reflects that the soft excitation is the main excitation process. In addition, the normalization constant N_0 increases with increase in energy and centrality, and decreases with increase in particle mass.

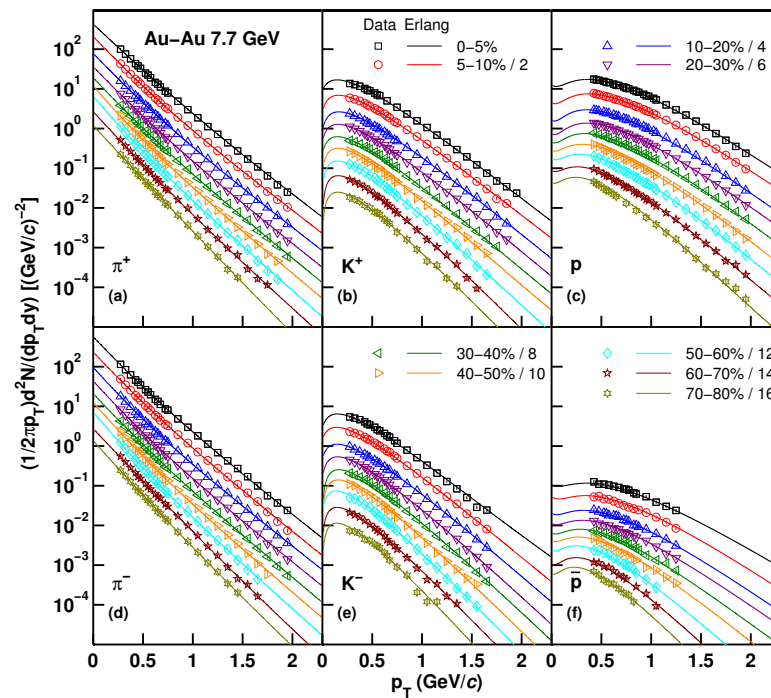


Figure 1. p_T spectra for (a–c) positive (π^+ , K^+ , p) and (d–f) negative (π^- , K^- , \bar{p}) particles produced in Au–Au collisions with $|y| < 0.1$ at $\sqrt{s_{NN}} = 7.7$ GeV for different centralities (0–5%, 5–10%, 10–20%, 20–30%, 30–40%, 40–50%, 50–60%, 60–70%, and 70–80%). The experimental data represented by the symbols are measured by the STAR Collaboration [33]. The spectra for different centralities are scaled by suitable factors for clarity. The plotted error bars include both statistical and systematic uncertainties, and the curves are the two-component Erlang distribution fits to the spectra.

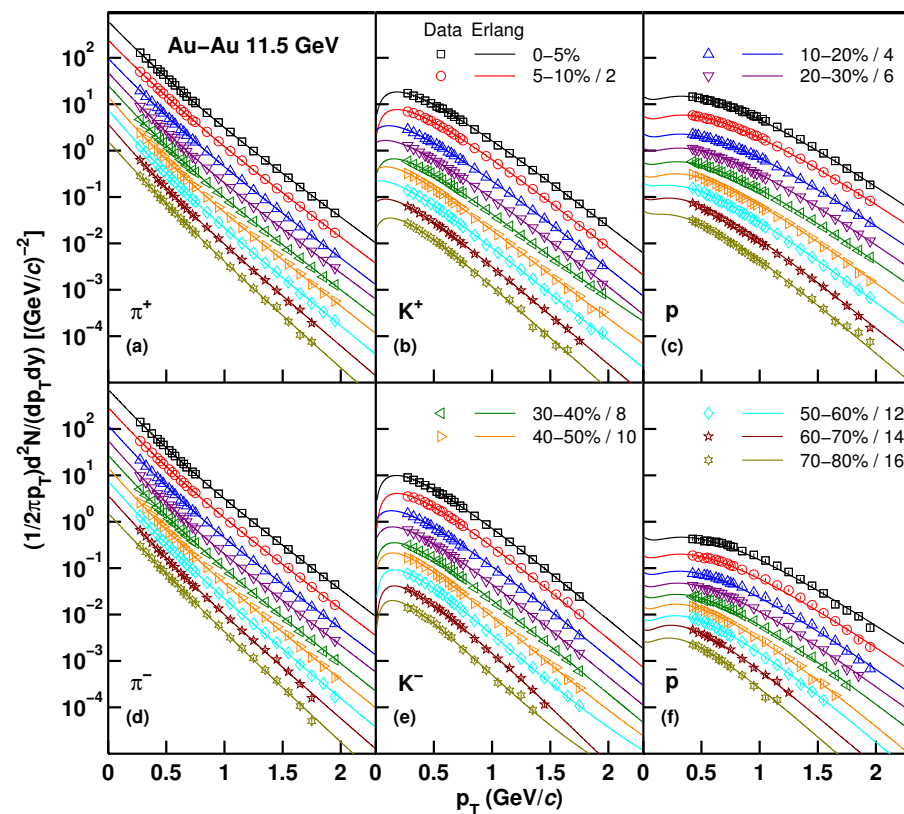


Figure 2. Same as Figure 1 but for Au–Au collisions at $\sqrt{s_{NN}} = 11.5$ GeV. The experimental data are from reference [33].

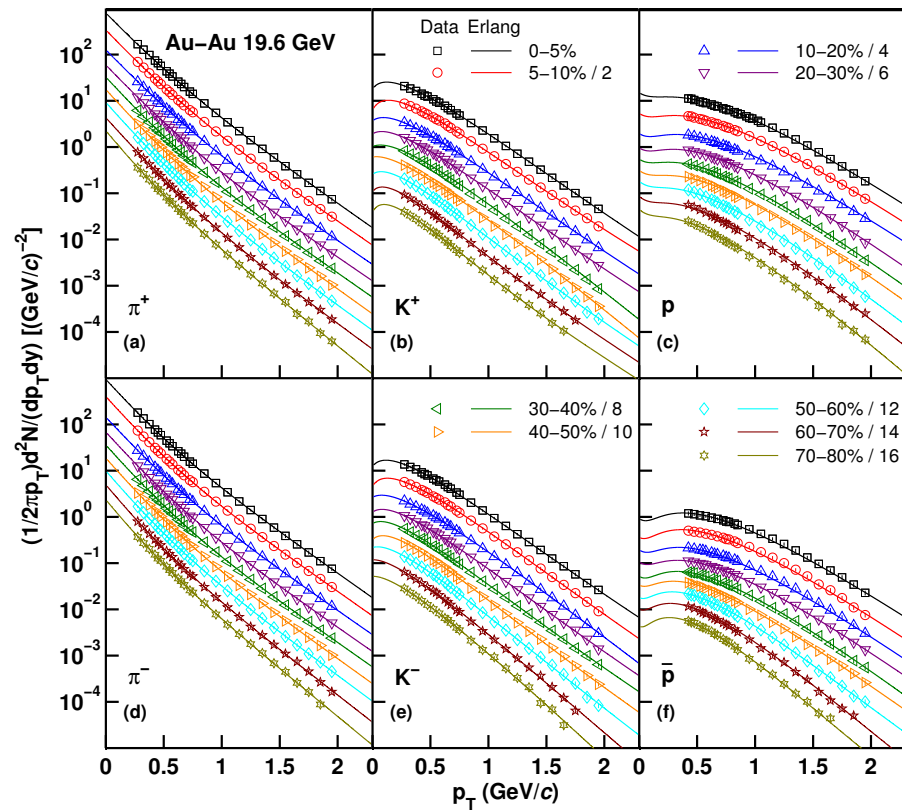


Figure 3. Same as in Figure 1 for Au-Au collisions at $\sqrt{s_{NN}} = 19.6$ GeV. The experimental data are from reference [33].

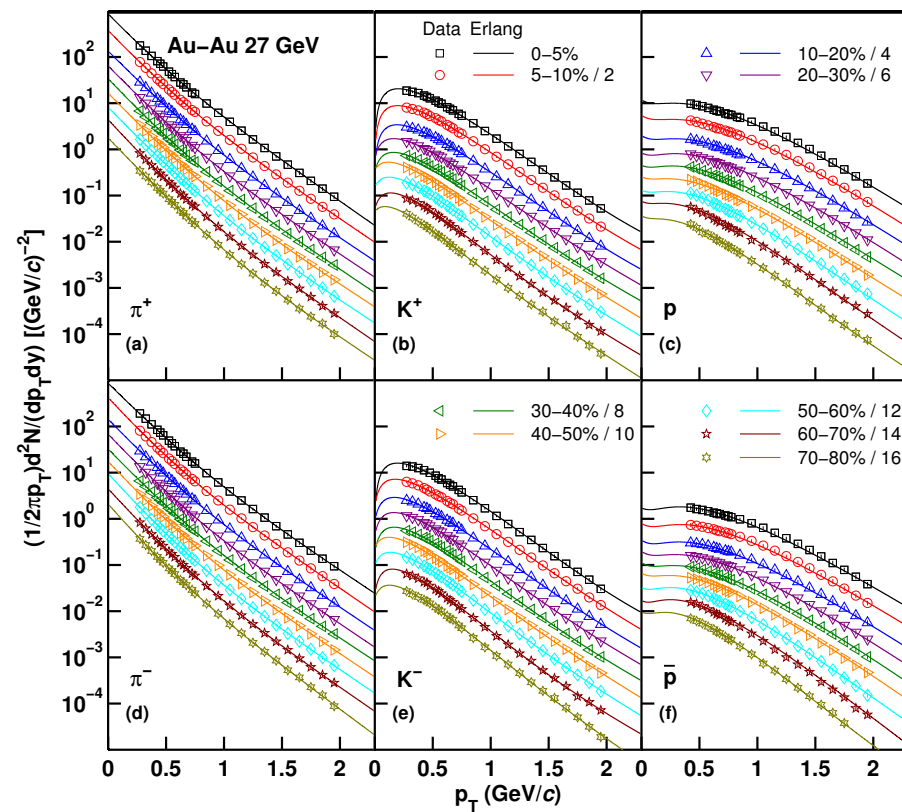


Figure 4. Same as Figure 1 for Au-Au collisions at $\sqrt{s_{NN}} = 27$ GeV. The experimental data are from reference [33].

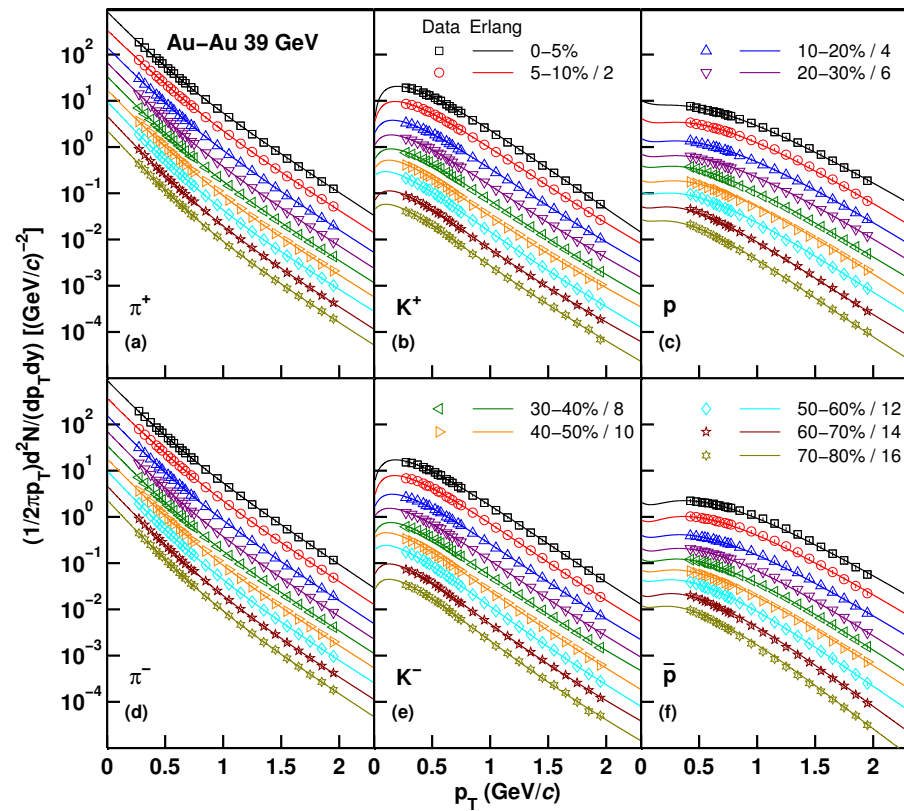


Figure 5. Same as Figure 1 for Au-Au collisions at $\sqrt{s_{NN}} = 39$ GeV. The experimental data are from reference [33].

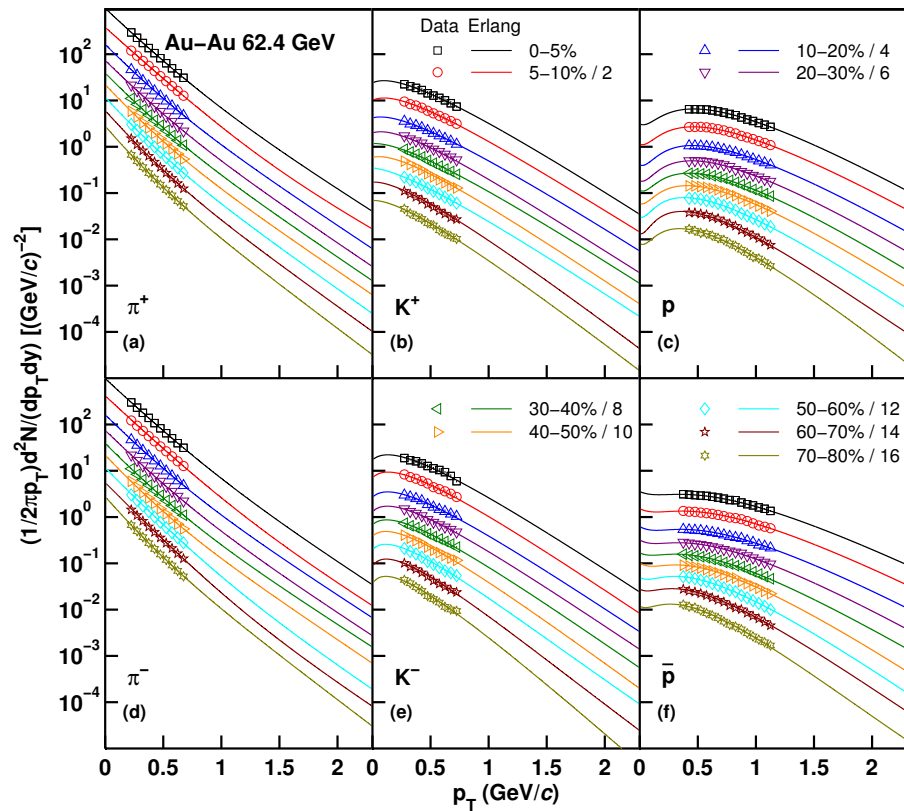


Figure 6. Same as Figure 1 for Au-Au collisions at $\sqrt{s_{NN}} = 62.4$ GeV. The experimental data were recorded by the STAR Collaboration [34].

Table 1. Values of free parameters, normalization constant, and χ^2/dof corresponding to the two-component Erlang p_T distribution for production in Au-Au collisions at $\sqrt{s_{NN}} = 7.7$ GeV for different centralities in Figure 1. (m_1 equals 2, 3, and 4 for π^\pm , K^\pm , and $p(\bar{p})$, respectively; m_2 equals 2 for all particles.)

Figure	Particle	Centrality	$\langle p_{t1} \rangle$ (GeV/c)	k_1	$\langle p_{t2} \rangle$ (GeV/c)	N_0	χ^2/dof
Figure 1a	π^+	0–5%	0.172 ± 0.004	0.63 ± 0.06	0.233 ± 0.004	96.122 ± 3.364	13.970/20
		5–10%	0.148 ± 0.006	0.51 ± 0.03	0.225 ± 0.002	80.050 ± 2.642	3.319/20
		10–20%	0.150 ± 0.006	0.51 ± 0.04	0.224 ± 0.003	60.889 ± 2.192	1.896/20
		20–30%	0.150 ± 0.006	0.51 ± 0.03	0.219 ± 0.002	41.772 ± 1.378	3.579/20
		30–40%	0.147 ± 0.006	0.51 ± 0.03	0.214 ± 0.003	28.090 ± 0.955	5.519/20
		40–50%	0.135 ± 0.005	0.51 ± 0.03	0.207 ± 0.003	18.994 ± 0.646	3.120/19
		50–60%	0.133 ± 0.006	0.51 ± 0.03	0.198 ± 0.003	11.956 ± 0.383	8.153/19
		60–70%	0.148 ± 0.004	0.59 ± 0.05	0.195 ± 0.003	6.225 ± 0.212	9.046/18
		70–80%	0.151 ± 0.004	0.53 ± 0.07	0.176 ± 0.004	3.125 ± 0.103	3.702/15
Figure 1d	π^-	0–5%	0.149 ± 0.006	0.52 ± 0.03	0.219 ± 0.003	107.122 ± 3.642	9.297/20
		5–10%	0.147 ± 0.006	0.51 ± 0.03	0.216 ± 0.002	86.526 ± 3.028	16.388/20
		10–20%	0.141 ± 0.007	0.51 ± 0.03	0.219 ± 0.002	67.409 ± 2.494	3.500/20
		20–30%	0.142 ± 0.006	0.51 ± 0.03	0.215 ± 0.003	45.954 ± 1.608	5.489/20
		30–40%	0.147 ± 0.007	0.51 ± 0.03	0.209 ± 0.003	30.232 ± 1.028	7.770/20
		40–50%	0.137 ± 0.006	0.51 ± 0.03	0.203 ± 0.003	20.251 ± 0.689	9.656/18
		50–60%	0.132 ± 0.006	0.51 ± 0.03	0.195 ± 0.002	12.950 ± 0.414	7.004/17
		60–70%	0.161 ± 0.003	0.83 ± 0.05	0.200 ± 0.006	6.606 ± 0.231	9.005/17
		70–80%	0.146 ± 0.004	0.61 ± 0.05	0.185 ± 0.004	3.438 ± 0.131	2.791/15
Figure 1b	K^+	0–5%	0.197 ± 0.003	0.81 ± 0.16	0.260 ± 0.018	20.070 ± 0.682	9.050/17
		5–10%	0.193 ± 0.003	0.86 ± 0.14	0.270 ± 0.024	16.565 ± 0.514	6.988/19
		10–20%	0.191 ± 0.002	0.86 ± 0.14	0.255 ± 0.017	12.444 ± 0.373	11.722/19
		20–30%	0.186 ± 0.002	0.87 ± 0.13	0.244 ± 0.016	8.508 ± 0.264	6.350/19
		30–40%	0.178 ± 0.003	0.85 ± 0.15	0.252 ± 0.016	5.111 ± 0.164	13.359/18
		40–50%	0.173 ± 0.003	0.86 ± 0.14	0.255 ± 0.043	3.150 ± 0.101	7.742/17
		50–60%	0.168 ± 0.002	0.90 ± 0.10	0.231 ± 0.032	1.721 ± 0.053	5.944/16
		60–70%	0.161 ± 0.002	0.92 ± 0.08	0.202 ± 0.040	0.800 ± 0.034	8.731/15
		70–80%	0.156 ± 0.003	0.91 ± 0.09	0.230 ± 0.046	0.330 ± 0.013	13.035/12
Figure 1e	K^-	0–5%	0.185 ± 0.004	0.89 ± 0.11	0.258 ± 0.015	7.208 ± 0.252	18.217/17
		5–10%	0.182 ± 0.003	0.82 ± 0.16	0.247 ± 0.018	6.131 ± 0.196	10.748/17
		10–20%	0.182 ± 0.002	0.86 ± 0.14	0.226 ± 0.024	4.620 ± 0.143	4.469/17
		20–30%	0.174 ± 0.002	0.92 ± 0.08	0.195 ± 0.039	3.129 ± 0.113	4.821/17
		30–40%	0.170 ± 0.002	0.95 ± 0.05	0.204 ± 0.040	1.990 ± 0.070	6.867/17
		40–50%	0.162 ± 0.002	0.90 ± 0.10	0.220 ± 0.044	1.243 ± 0.044	8.169/14
		50–60%	0.155 ± 0.002	0.90 ± 0.10	0.195 ± 0.034	0.692 ± 0.027	12.526/15
		60–70%	0.152 ± 0.003	0.90 ± 0.10	0.218 ± 0.043	0.312 ± 0.011	12.456/13
		70–80%	0.146 ± 0.004	0.91 ± 0.09	0.180 ± 0.036	0.133 ± 0.006	27.764/10
Figure 1c	p	0–5%	0.215 ± 0.003	0.89 ± 0.08	0.270 ± 0.054	52.211 ± 2.193	4.927/23
		5–10%	0.211 ± 0.003	0.91 ± 0.08	0.265 ± 0.053	44.223 ± 1.946	3.353/23
		10–20%	0.201 ± 0.003	0.91 ± 0.09	0.265 ± 0.053	32.020 ± 1.473	9.462/23
		20–30%	0.200 ± 0.003	0.92 ± 0.08	0.250 ± 0.050	21.932 ± 0.855	2.729/23
		30–40%	0.192 ± 0.003	0.90 ± 0.09	0.250 ± 0.050	14.565 ± 0.612	4.083/22
		40–50%	0.183 ± 0.003	0.86 ± 0.09	0.260 ± 0.035	8.745 ± 0.350	4.582/22
		50–60%	0.174 ± 0.003	0.83 ± 0.14	0.260 ± 0.035	5.248 ± 0.210	18.492/21
		60–70%	0.164 ± 0.003	0.80 ± 0.16	0.260 ± 0.019	2.622 ± 0.105	13.162/22
		70–80%	0.154 ± 0.002	0.71 ± 0.16	0.200 ± 0.016	1.345 ± 0.059	12.753/15
Figure 1f	\bar{p}	0–5%	0.232 ± 0.011	0.81 ± 0.16	0.334 ± 0.066	0.392 ± 0.019	3.384/9
		5–10%	0.217 ± 0.009	0.87 ± 0.13	0.247 ± 0.049	0.338 ± 0.016	7.632/8
		10–20%	0.205 ± 0.009	0.82 ± 0.11	0.302 ± 0.060	0.257 ± 0.012	3.345/12
		20–30%	0.198 ± 0.009	0.80 ± 0.16	0.310 ± 0.062	0.202 ± 0.009	9.058/10
		30–40%	0.184 ± 0.008	0.79 ± 0.15	0.300 ± 0.060	0.140 ± 0.007	3.650/11
		40–50%	0.174 ± 0.006	0.81 ± 0.16	0.266 ± 0.053	0.099 ± 0.006	8.561/8
		50–60%	0.156 ± 0.007	0.79 ± 0.15	0.260 ± 0.052	0.058 ± 0.003	5.627/7
		60–70%	0.148 ± 0.007	0.83 ± 0.16	0.236 ± 0.047	0.031 ± 0.002	4.186/5
		70–80%	0.137 ± 0.011	0.82 ± 0.16	0.224 ± 0.044	0.017 ± 0.002	1.189/3

Table 2. Values of free parameters, normalization constant, and χ^2/dof corresponding to the two-component Erlang p_T distribution for production in Au-Au collisions at $\sqrt{s_{NN}} = 11.5 \text{ GeV}$ for different centralities in Figure 2. (m_1 equals 2, 3, and 4 for π^\pm , K^\pm , and $p(\bar{p})$, respectively; m_2 equals 2 for all particles.)

Figure	Particle	Centrality	$\langle p_{t1} \rangle$ (GeV/c)	k_1	$\langle p_{t2} \rangle$ (GeV/c)	N_0	χ^2/dof
Figure 2a	π^+	0–5%	0.153 ± 0.007	0.52 ± 0.04	0.236 ± 0.003	125.208 ± 4.633	2.186/20
		5–10%	0.153 ± 0.006	0.51 ± 0.04	0.233 ± 0.003	98.692 ± 3.257	1.584/20
		10–20%	0.149 ± 0.007	0.51 ± 0.03	0.230 ± 0.003	76.333 ± 3.053	1.429/20
		20–30%	0.143 ± 0.006	0.53 ± 0.04	0.233 ± 0.003	52.743 ± 1.846	1.146/20
		30–40%	0.141 ± 0.006	0.53 ± 0.04	0.227 ± 0.003	36.192 ± 1.231	0.998/20
		40–50%	0.133 ± 0.006	0.51 ± 0.03	0.221 ± 0.003	23.473 ± 0.845	1.222/20
		50–60%	0.132 ± 0.006	0.51 ± 0.03	0.212 ± 0.002	14.263 ± 0.571	2.065/20
		60–70%	0.133 ± 0.006	0.51 ± 0.03	0.204 ± 0.003	8.159 ± 0.310	2.188/18
70–80%	0.141 ± 0.006	0.52 ± 0.04	0.197 ± 0.003	4.135 ± 0.141	5.479/18		
Figure 2d	π^-	0–5%	0.146 ± 0.008	0.51 ± 0.04	0.230 ± 0.003	135.170 ± 5.812	1.593/20
		5–10%	0.143 ± 0.007	0.51 ± 0.04	0.229 ± 0.002	107.425 ± 4.082	1.383/20
		10–20%	0.140 ± 0.005	0.53 ± 0.04	0.230 ± 0.003	83.065 ± 2.658	0.781/20
		20–30%	0.135 ± 0.006	0.51 ± 0.04	0.227 ± 0.003	56.923 ± 1.992	0.895/20
		30–40%	0.140 ± 0.006	0.51 ± 0.03	0.220 ± 0.003	38.112 ± 1.334	2.378/20
		40–50%	0.137 ± 0.007	0.51 ± 0.03	0.216 ± 0.003	24.354 ± 0.950	4.048/20
		50–60%	0.137 ± 0.006	0.51 ± 0.03	0.209 ± 0.003	14.725 ± 0.560	7.309/20
		60–70%	0.139 ± 0.005	0.51 ± 0.03	0.201 ± 0.003	8.447 ± 0.287	11.989/18
70–80%	0.150 ± 0.005	0.51 ± 0.04	0.191 ± 0.003	4.250 ± 0.153	10.734/18		
Figure 2b	K^+	0–5%	0.201 ± 0.003	0.88 ± 0.12	0.262 ± 0.048	24.436 ± 0.733	1.486/19
		5–10%	0.198 ± 0.002	0.94 ± 0.06	0.207 ± 0.041	19.832 ± 0.714	2.160/20
		10–20%	0.200 ± 0.002	0.82 ± 0.06	0.199 ± 0.026	14.781 ± 0.473	2.322/20
		20–30%	0.199 ± 0.003	0.76 ± 0.06	0.205 ± 0.020	9.726 ± 0.350	3.432/20
		30–40%	0.184 ± 0.003	0.79 ± 0.05	0.306 ± 0.010	5.985 ± 0.180	1.553/20
		40–50%	0.174 ± 0.003	0.59 ± 0.09	0.260 ± 0.007	3.861 ± 0.131	5.020/20
		50–60%	0.180 ± 0.003	0.54 ± 0.10	0.236 ± 0.006	2.000 ± 0.060	5.888/19
		60–70%	0.172 ± 0.003	0.65 ± 0.13	0.228 ± 0.009	0.997 ± 0.033	2.330/17
70–80%	0.163 ± 0.003	0.78 ± 0.15	0.231 ± 0.016	0.464 ± 0.015	11.598/16		
Figure 2e	K^-	0–5%	0.191 ± 0.003	0.93 ± 0.07	0.221 ± 0.044	12.017 ± 0.385	1.338/17
		5–10%	0.188 ± 0.002	0.94 ± 0.06	0.295 ± 0.059	9.851 ± 0.325	7.987/18
		10–20%	0.193 ± 0.003	0.83 ± 0.16	0.219 ± 0.022	7.509 ± 0.225	10.112/18
		20–30%	0.185 ± 0.003	0.82 ± 0.16	0.245 ± 0.018	4.915 ± 0.152	3.830/18
		30–40%	0.182 ± 0.002	0.88 ± 0.11	0.256 ± 0.015	3.046 ± 0.091	3.806/17
		40–50%	0.167 ± 0.003	0.82 ± 0.06	0.275 ± 0.010	1.974 ± 0.069	4.685/17
		50–60%	0.164 ± 0.003	0.92 ± 0.04	0.327 ± 0.027	1.031 ± 0.032	4.597/17
		60–70%	0.162 ± 0.003	0.92 ± 0.08	0.254 ± 0.050	0.517 ± 0.019	5.856/14
70–80%	0.148 ± 0.004	0.91 ± 0.06	0.325 ± 0.046	0.246 ± 0.010	14.250/10		
Figure 2c	p	0–5%	0.213 ± 0.004	0.88 ± 0.08	0.234 ± 0.046	42.924 ± 1.803	8.894/22
		5–10%	0.214 ± 0.005	0.89 ± 0.10	0.230 ± 0.046	34.265 ± 1.508	1.597/23
		10–20%	0.211 ± 0.004	0.88 ± 0.08	0.228 ± 0.045	25.603 ± 1.203	1.361/23
		20–30%	0.205 ± 0.004	0.85 ± 0.12	0.250 ± 0.050	17.849 ± 0.696	6.665/23
		30–40%	0.200 ± 0.004	0.80 ± 0.16	0.285 ± 0.038	11.424 ± 0.434	5.483/23
		40–50%	0.189 ± 0.003	0.80 ± 0.16	0.275 ± 0.029	7.038 ± 0.282	11.643/22
		50–60%	0.179 ± 0.003	0.70 ± 0.14	0.286 ± 0.017	4.076 ± 0.167	12.886/22
		60–70%	0.171 ± 0.003	0.62 ± 0.14	0.230 ± 0.010	2.208 ± 0.097	14.500/22
70–80%	0.161 ± 0.003	0.69 ± 0.13	0.246 ± 0.015	0.995 ± 0.040	24.989/23		
Figure 2f	\bar{p}	0–5%	0.216 ± 0.003	0.88 ± 0.08	0.234 ± 0.046	1.374 ± 0.066	23.483/17
		5–10%	0.209 ± 0.005	0.84 ± 0.14	0.273 ± 0.054	1.098 ± 0.047	21.419/17
		10–20%	0.203 ± 0.004	0.85 ± 0.10	0.253 ± 0.050	0.888 ± 0.039	24.352/17
		20–30%	0.196 ± 0.004	0.83 ± 0.13	0.265 ± 0.045	0.687 ± 0.030	8.201/17
		30–40%	0.189 ± 0.004	0.86 ± 0.09	0.229 ± 0.045	0.491 ± 0.022	4.604/17
		40–50%	0.176 ± 0.003	0.87 ± 0.09	0.214 ± 0.042	0.331 ± 0.016	5.954/14
		50–60%	0.172 ± 0.004	0.85 ± 0.11	0.228 ± 0.045	0.213 ± 0.010	3.503/13
		60–70%	0.155 ± 0.004	0.77 ± 0.15	0.261 ± 0.034	0.127 ± 0.005	3.407/8
70–80%	0.147 ± 0.008	0.74 ± 0.14	0.256 ± 0.051	0.069 ± 0.003	7.499/8		

Table 3. Values of free parameters, normalization constant, and χ^2/dof corresponding to the two-component Erlang p_T distribution for production in Au-Au collisions at $\sqrt{s_{NN}} = 19.6\text{ GeV}$ for different centralities in Figure 3. (m_1 equals 2, 3, and 4 for π^\pm , K^\pm , and $p(\bar{p})$, respectively; m_2 equals 2 for all particles.)

Figure	Particle	Centrality	$\langle p_{t1} \rangle$ (GeV/c)	k_1	$\langle p_{t2} \rangle$ (GeV/c)	N_0	χ^2/dof
Figure 3a	π^+	0–5%	0.156 ± 0.008	0.57 ± 0.05	0.249 ± 0.005	165.077 ± 8.089	0.737/20
		5–10%	0.155 ± 0.007	0.61 ± 0.04	0.253 ± 0.005	136.482 ± 5.732	0.519/20
		10–20%	0.158 ± 0.006	0.63 ± 0.04	0.255 ± 0.004	103.435 ± 4.137	0.375/20
		20–30%	0.157 ± 0.006	0.66 ± 0.03	0.257 ± 0.005	70.526 ± 2.962	0.431/20
		30–40%	0.150 ± 0.005	0.64 ± 0.04	0.250 ± 0.004	48.064 ± 1.730	0.625/20
		40–50%	0.145 ± 0.005	0.63 ± 0.04	0.244 ± 0.004	30.629 ± 1.072	1.211/20
		50–60%	0.144 ± 0.005	0.65 ± 0.03	0.241 ± 0.004	18.732 ± 0.693	1.247/20
		60–70%	0.147 ± 0.005	0.68 ± 0.03	0.238 ± 0.004	10.253 ± 0.390	0.759/20
	70–80%	0.131 ± 0.006	0.53 ± 0.03	0.214 ± 0.003	5.523 ± 0.232	2.812/20	
Figure 3d	π^-	0–5%	0.145 ± 0.008	0.56 ± 0.04	0.246 ± 0.004	176.077 ± 8.452	0.682/20
		5–10%	0.144 ± 0.007	0.58 ± 0.04	0.247 ± 0.004	145.211 ± 6.244	0.511/20
		10–20%	0.150 ± 0.007	0.61 ± 0.04	0.251 ± 0.005	108.850 ± 5.007	0.342/20
		20–30%	0.147 ± 0.005	0.62 ± 0.04	0.250 ± 0.005	74.545 ± 2.684	1.105/20
		30–40%	0.145 ± 0.005	0.63 ± 0.04	0.248 ± 0.005	50.278 ± 1.860	0.946/20
		40–50%	0.143 ± 0.005	0.63 ± 0.03	0.243 ± 0.003	31.803 ± 1.177	1.114/20
		50–60%	0.139 ± 0.005	0.61 ± 0.03	0.235 ± 0.003	19.461 ± 0.681	0.970/20
		60–70%	0.133 ± 0.006	0.56 ± 0.03	0.223 ± 0.003	10.814 ± 0.411	2.663/20
	70–80%	0.129 ± 0.005	0.51 ± 0.03	0.211 ± 0.002	5.709 ± 0.183	3.269/19	
Figure 3b	K^+	0–5%	0.198 ± 0.005	0.67 ± 0.13	0.294 ± 0.009	29.706 ± 0.891	1.316/20
		5–10%	0.192 ± 0.005	0.68 ± 0.07	0.315 ± 0.007	24.335 ± 0.973	1.187/20
		10–20%	0.192 ± 0.006	0.57 ± 0.10	0.291 ± 0.008	18.218 ± 0.619	1.652/20
		20–30%	0.186 ± 0.006	0.53 ± 0.09	0.285 ± 0.005	12.546 ± 0.452	1.466/20
		30–40%	0.198 ± 0.002	0.69 ± 0.13	0.223 ± 0.009	8.233 ± 0.255	26.212/20
		40–50%	0.194 ± 0.002	0.63 ± 0.12	0.220 ± 0.007	4.992 ± 0.155	13.256/19
		50–60%	0.165 ± 0.005	0.51 ± 0.05	0.266 ± 0.004	2.790 ± 0.089	3.925/19
		60–70%	0.152 ± 0.005	0.51 ± 0.04	0.269 ± 0.005	1.417 ± 0.054	1.169/17
	70–80%	0.148 ± 0.004	0.57 ± 0.05	0.274 ± 0.006	0.680 ± 0.023	2.210/16	
Figure 3e	K^-	0–5%	0.192 ± 0.004	0.64 ± 0.07	0.292 ± 0.007	18.620 ± 0.596	2.950/20
		5–10%	0.193 ± 0.003	0.70 ± 0.09	0.284 ± 0.006	15.498 ± 0.527	1.836/20
		10–20%	0.199 ± 0.003	0.65 ± 0.13	0.248 ± 0.008	11.714 ± 0.375	1.861/20
		20–30%	0.183 ± 0.005	0.56 ± 0.08	0.274 ± 0.005	8.148 ± 0.253	2.810/20
		30–40%	0.174 ± 0.005	0.51 ± 0.09	0.270 ± 0.004	5.358 ± 0.166	2.310/20
		40–50%	0.170 ± 0.004	0.58 ± 0.06	0.262 ± 0.004	3.299 ± 0.102	4.047/19
		50–60%	0.170 ± 0.004	0.51 ± 0.10	0.240 ± 0.005	1.920 ± 0.060	8.328/19
		60–70%	0.172 ± 0.003	0.51 ± 0.10	0.216 ± 0.006	0.991 ± 0.035	8.495/17
	70–80%	0.172 ± 0.003	0.65 ± 0.05	0.178 ± 0.011	0.472 ± 0.015	10.403/15	
Figure 3c	p	0–5%	0.222 ± 0.005	0.79 ± 0.11	0.278 ± 0.055	34.690 ± 1.353	6.636/23
		5–10%	0.221 ± 0.004	0.84 ± 0.08	0.261 ± 0.052	28.720 ± 1.120	3.465/19
		10–20%	0.220 ± 0.003	0.85 ± 0.15	0.261 ± 0.052	22.471 ± 0.921	13.856/17
		20–30%	0.208 ± 0.003	0.84 ± 0.07	0.250 ± 0.050	14.238 ± 0.541	3.297/17
		30–40%	0.202 ± 0.003	0.81 ± 0.10	0.250 ± 0.038	9.105 ± 0.355	4.214/17
		40–50%	0.201 ± 0.003	0.82 ± 0.14	0.229 ± 0.044	5.738 ± 0.258	11.385/17
		50–60%	0.191 ± 0.003	0.81 ± 0.16	0.212 ± 0.042	3.252 ± 0.140	17.833/17
		60–70%	0.185 ± 0.003	0.82 ± 0.09	0.200 ± 0.040	1.684 ± 0.082	17.194/17
	70–80%	0.175 ± 0.003	0.78 ± 0.09	0.200 ± 0.032	0.818 ± 0.038	18.275/17	
Figure 3f	\bar{p}	0–5%	0.222 ± 0.004	0.91 ± 0.08	0.247 ± 0.049	3.937 ± 0.161	11.586/16
		5–10%	0.215 ± 0.003	0.88 ± 0.11	0.290 ± 0.058	3.204 ± 0.131	15.482/16
		10–20%	0.213 ± 0.004	0.89 ± 0.10	0.240 ± 0.048	2.562 ± 0.120	12.446/18
		20–30%	0.209 ± 0.004	0.88 ± 0.11	0.240 ± 0.048	1.926 ± 0.089	2.372/18
		30–40%	0.199 ± 0.003	0.88 ± 0.08	0.249 ± 0.049	1.355 ± 0.066	1.118/19
		40–50%	0.190 ± 0.004	0.78 ± 0.15	0.313 ± 0.029	0.940 ± 0.038	3.909/19
		50–60%	0.177 ± 0.003	0.79 ± 0.15	0.300 ± 0.018	0.586 ± 0.028	1.950/19
		60–70%	0.167 ± 0.003	0.81 ± 0.15	0.268 ± 0.023	0.340 ± 0.014	7.299/17
	70–80%	0.155 ± 0.003	0.81 ± 0.14	0.271 ± 0.033	0.169 ± 0.007	4.949/16	

Table 4. Values of free parameters, normalization constant, and χ^2/dof corresponding to the two-component Erlang p_T distribution for production in Au-Au collisions at $\sqrt{s_{NN}} = 27$ GeV for different centralities in Figure 4. (m_1 equals 2, 3, and 4 for π^\pm , K^\pm , and $p(\bar{p})$, respectively; m_2 equals 2 for all particles.)

Figure	Particle	Centrality	$\langle p_{t1} \rangle$ (GeV/c)	k_1	$\langle p_{t2} \rangle$ (GeV/c)	N_0	χ^2/dof
Figure 4a	π^+	0–5%	0.152 ± 0.007	0.51 ± 0.05	0.249 ± 0.003	182.402 ± 6.202	2.449/20
		5–10%	0.155 ± 0.007	0.60 ± 0.04	0.257 ± 0.005	153.577 ± 6.911	0.311/20
		10–20%	0.161 ± 0.007	0.64 ± 0.04	0.263 ± 0.005	114.051 ± 4.676	0.277/20
		20–30%	0.158 ± 0.007	0.65 ± 0.04	0.263 ± 0.005	78.449 ± 3.060	0.423/20
		30–40%	0.155 ± 0.005	0.66 ± 0.04	0.261 ± 0.005	52.828 ± 2.007	0.615/20
		40–50%	0.160 ± 0.005	0.72 ± 0.03	0.268 ± 0.006	32.638 ± 1.338	0.568/20
		50–60%	0.161 ± 0.005	0.74 ± 0.03	0.267 ± 0.005	19.253 ± 0.712	0.489/20
		60–70%	0.152 ± 0.004	0.71 ± 0.03	0.255 ± 0.004	11.041 ± 0.353	0.909/20
		70–80%	0.160 ± 0.004	0.79 ± 0.02	0.264 ± 0.004	5.287 ± 0.169	1.377/20
Figure 4d	π^-	0–5%	0.164 ± 0.006	0.66 ± 0.04	0.264 ± 0.004	186.402 ± 6.710	2.325/20
		5–10%	0.149 ± 0.007	0.60 ± 0.04	0.255 ± 0.005	160.852 ± 6.273	0.452/20
		10–20%	0.157 ± 0.007	0.63 ± 0.04	0.261 ± 0.005	117.063 ± 4.800	0.337/20
		20–30%	0.154 ± 0.006	0.63 ± 0.04	0.259 ± 0.005	80.615 ± 2.983	0.418/20
		30–40%	0.160 ± 0.005	0.69 ± 0.03	0.267 ± 0.006	52.364 ± 1.676	0.442/20
		40–50%	0.155 ± 0.006	0.68 ± 0.03	0.261 ± 0.005	33.302 ± 1.565	0.349/20
		50–60%	0.150 ± 0.005	0.69 ± 0.03	0.257 ± 0.005	20.431 ± 0.797	0.675/20
		60–70%	0.152 ± 0.006	0.71 ± 0.03	0.254 ± 0.005	11.201 ± 0.538	0.358/20
		70–80%	0.144 ± 0.005	0.64 ± 0.03	0.235 ± 0.003	5.647 ± 0.209	1.634/20
Figure 4b	K^+	0–5%	0.205 ± 0.004	0.97 ± 0.02	0.575 ± 0.115	29.993 ± 0.930	1.988/20
		5–10%	0.201 ± 0.003	0.94 ± 0.02	0.462 ± 0.030	24.959 ± 0.799	2.304/20
		10–20%	0.199 ± 0.003	0.92 ± 0.03	0.430 ± 0.028	18.851 ± 0.547	2.702/20
		20–30%	0.191 ± 0.004	0.77 ± 0.05	0.349 ± 0.010	12.830 ± 0.398	1.806/20
		30–40%	0.186 ± 0.004	0.77 ± 0.03	0.348 ± 0.006	8.241 ± 0.247	2.330/20
		40–50%	0.174 ± 0.004	0.60 ± 0.05	0.307 ± 0.006	5.274 ± 0.185	1.779/20
		50–60%	0.171 ± 0.005	0.64 ± 0.05	0.305 ± 0.006	2.935 ± 0.091	2.899/20
		60–70%	0.165 ± 0.003	0.72 ± 0.03	0.313 ± 0.007	1.512 ± 0.045	4.541/20
		70–80%	0.152 ± 0.005	0.51 ± 0.05	0.276 ± 0.004	0.702 ± 0.022	4.851/20
Figure 4e	K^-	0–5%	0.198 ± 0.002	0.97 ± 0.01	0.531 ± 0.052	21.872 ± 0.634	5.463/19
		5–10%	0.192 ± 0.003	0.85 ± 0.03	0.357 ± 0.012	18.306 ± 0.567	2.210/20
		10–20%	0.188 ± 0.003	0.82 ± 0.04	0.351 ± 0.010	14.220 ± 0.427	2.037/20
		20–30%	0.185 ± 0.003	0.81 ± 0.03	0.347 ± 0.008	9.713 ± 0.291	2.793/20
		30–40%	0.183 ± 0.003	0.83 ± 0.03	0.353 ± 0.009	6.140 ± 0.196	3.571/20
		40–50%	0.172 ± 0.004	0.65 ± 0.05	0.302 ± 0.005	3.911 ± 0.121	2.514/20
		50–60%	0.169 ± 0.004	0.70 ± 0.04	0.303 ± 0.005	2.185 ± 0.076	2.350/20
		60–70%	0.166 ± 0.003	0.82 ± 0.03	0.329 ± 0.009	1.101 ± 0.034	4.562/20
		70–80%	0.163 ± 0.004	0.72 ± 0.05	0.276 ± 0.008	0.512 ± 0.016	12.189/20
Figure 4c	p	0–5%	0.226 ± 0.005	0.80 ± 0.16	0.284 ± 0.056	30.191 ± 1.328	8.619/17
		5–10%	0.222 ± 0.005	0.82 ± 0.10	0.261 ± 0.052	26.024 ± 1.093	7.610/17
		10–20%	0.222 ± 0.004	0.83 ± 0.10	0.261 ± 0.052	20.160 ± 0.887	4.736/17
		20–30%	0.216 ± 0.004	0.78 ± 0.15	0.308 ± 0.035	13.750 ± 0.577	9.822/17
		30–40%	0.206 ± 0.004	0.70 ± 0.14	0.345 ± 0.022	9.066 ± 0.381	13.078/17
		40–50%	0.196 ± 0.006	0.65 ± 0.13	0.339 ± 0.020	5.287 ± 0.248	2.337/17
		50–60%	0.185 ± 0.004	0.67 ± 0.13	0.318 ± 0.018	3.037 ± 0.118	6.823/17
		60–70%	0.175 ± 0.004	0.64 ± 0.12	0.305 ± 0.013	1.725 ± 0.069	23.466/17
		70–80%	0.160 ± 0.004	0.57 ± 0.08	0.293 ± 0.008	0.733 ± 0.029	5.857/17
Figure 4f	\bar{p}	0–5%	0.228 ± 0.006	0.78 ± 0.15	0.343 ± 0.059	5.877 ± 0.235	12.404/16
		5–10%	0.228 ± 0.005	0.86 ± 0.10	0.260 ± 0.052	4.869 ± 0.234	9.255/16
		10–20%	0.222 ± 0.004	0.87 ± 0.12	0.240 ± 0.048	3.884 ± 0.179	8.533/16
		20–30%	0.217 ± 0.004	0.85 ± 0.14	0.241 ± 0.048	2.900 ± 0.122	1.710/16
		30–40%	0.210 ± 0.003	0.83 ± 0.13	0.249 ± 0.047	2.072 ± 0.085	1.695/16
		40–50%	0.200 ± 0.004	0.74 ± 0.14	0.295 ± 0.025	1.399 ± 0.062	1.579/16
		50–60%	0.185 ± 0.004	0.73 ± 0.14	0.300 ± 0.017	0.820 ± 0.032	2.232/16
		60–70%	0.177 ± 0.003	0.76 ± 0.15	0.277 ± 0.017	0.482 ± 0.021	21.340/16
		70–80%	0.157 ± 0.003	0.67 ± 0.13	0.278 ± 0.012	0.229 ± 0.009	4.569/14

Table 5. Values of free parameters, normalization constant, and χ^2/dof corresponding to the two-component Erlang p_T distribution for production in Au-Au collisions at $\sqrt{s_{NN}} = 39$ GeV for different centralities in Figure 5. (m_1 equals 2, 3, and 4 for π^\pm , K^\pm , and $p(\bar{p})$, respectively; m_2 equals 2 for all particles.)

Figure	Particle	Centrality	$\langle p_{t1} \rangle$ (GeV/c)	k_1	$\langle p_{t2} \rangle$ (GeV/c)	N_0	χ^2/dof
Figure 5a	π^+	0–5%	0.155 ± 0.008	0.54 ± 0.05	0.265 ± 0.004	185.159 ± 7.406	$3.265/20$
		5–10%	0.166 ± 0.007	0.63 ± 0.04	0.274 ± 0.006	153.984 ± 6.159	$0.386/20$
		10–20%	0.158 ± 0.008	0.61 ± 0.04	0.270 ± 0.005	121.765 ± 6.332	$0.376/20$
		20–30%	0.157 ± 0.008	0.63 ± 0.04	0.272 ± 0.005	83.486 ± 4.091	$0.484/20$
		30–40%	0.158 ± 0.007	0.66 ± 0.04	0.275 ± 0.006	54.946 ± 2.692	$0.493/20$
		40–50%	0.160 ± 0.006	0.70 ± 0.03	0.279 ± 0.006	34.963 ± 1.538	$0.577/20$
		50–60%	0.156 ± 0.004	0.72 ± 0.03	0.279 ± 0.006	21.974 ± 0.769	$0.740/20$
		60–70%	0.154 ± 0.005	0.72 ± 0.03	0.273 ± 0.005	12.108 ± 0.533	$0.446/20$
Figure 5d	π^-	0–5%	0.153 ± 0.010	0.53 ± 0.04	0.258 ± 0.004	191.409 ± 7.274	$1.089/20$
		5–10%	0.159 ± 0.008	0.60 ± 0.04	0.266 ± 0.006	159.491 ± 7.975	$0.233/20$
		10–20%	0.152 ± 0.008	0.59 ± 0.04	0.264 ± 0.005	126.386 ± 6.446	$0.306/20$
		20–30%	0.155 ± 0.007	0.63 ± 0.04	0.269 ± 0.005	85.965 ± 4.298	$0.365/20$
		30–40%	0.156 ± 0.007	0.65 ± 0.04	0.271 ± 0.006	56.262 ± 2.869	$0.355/20$
		40–50%	0.158 ± 0.006	0.69 ± 0.03	0.274 ± 0.006	35.958 ± 1.654	$0.376/20$
		50–60%	0.155 ± 0.006	0.71 ± 0.03	0.273 ± 0.006	22.498 ± 1.080	$0.483/20$
		60–70%	0.156 ± 0.006	0.73 ± 0.03	0.273 ± 0.005	12.258 ± 0.576	$0.425/20$
Figure 5b	K^+	0–5%	0.211 ± 0.003	0.94 ± 0.06	0.359 ± 0.045	31.219 ± 1.030	$5.650/20$
		5–10%	0.202 ± 0.004	0.83 ± 0.05	0.369 ± 0.014	27.111 ± 0.840	$1.564/20$
		10–20%	0.198 ± 0.005	0.73 ± 0.06	0.349 ± 0.010	20.074 ± 0.642	$1.340/20$
		20–30%	0.191 ± 0.006	0.67 ± 0.06	0.345 ± 0.009	13.603 ± 0.422	$2.281/20$
		30–40%	0.189 ± 0.005	0.68 ± 0.05	0.337 ± 0.006	8.778 ± 0.255	$2.462/20$
		40–50%	0.174 ± 0.006	0.60 ± 0.05	0.335 ± 0.008	5.514 ± 0.210	$1.220/20$
		50–60%	0.168 ± 0.006	0.51 ± 0.06	0.304 ± 0.004	3.273 ± 0.098	$2.751/20$
		60–70%	0.170 ± 0.004	0.63 ± 0.04	0.330 ± 0.006	1.605 ± 0.048	$2.878/20$
Figure 5e	K^-	0–5%	0.206 ± 0.003	0.86 ± 0.06	0.352 ± 0.020	24.658 ± 0.715	$5.446/20$
		5–10%	0.199 ± 0.004	0.83 ± 0.05	0.354 ± 0.014	21.186 ± 0.678	$3.110/20$
		10–20%	0.195 ± 0.005	0.73 ± 0.05	0.339 ± 0.009	15.792 ± 0.553	$2.063/20$
		20–30%	0.190 ± 0.006	0.65 ± 0.07	0.321 ± 0.008	10.783 ± 0.356	$2.454/20$
		30–40%	0.185 ± 0.005	0.68 ± 0.05	0.333 ± 0.006	7.005 ± 0.224	$1.989/20$
		40–50%	0.176 ± 0.005	0.56 ± 0.05	0.301 ± 0.005	4.478 ± 0.134	$2.504/20$
		50–60%	0.169 ± 0.005	0.55 ± 0.05	0.294 ± 0.005	2.666 ± 0.080	$2.100/20$
		60–70%	0.168 ± 0.004	0.66 ± 0.04	0.317 ± 0.005	1.316 ± 0.039	$3.159/20$
Figure 5c	p	0–5%	0.239 ± 0.005	0.79 ± 0.09	0.293 ± 0.055	26.115 ± 1.097	$3.078/16$
		5–10%	0.229 ± 0.004	0.86 ± 0.08	0.240 ± 0.048	22.026 ± 1.035	$4.637/16$
		10–20%	0.229 ± 0.006	0.82 ± 0.10	0.281 ± 0.056	17.136 ± 0.788	$1.181/16$
		20–30%	0.226 ± 0.006	0.80 ± 0.16	0.298 ± 0.059	12.027 ± 0.469	$5.461/16$
		30–40%	0.209 ± 0.006	0.69 ± 0.13	0.355 ± 0.032	8.191 ± 0.360	$10.732/16$
		40–50%	0.209 ± 0.004	0.75 ± 0.15	0.318 ± 0.032	4.934 ± 0.227	$13.569/16$
		50–60%	0.196 ± 0.005	0.67 ± 0.13	0.341 ± 0.026	2.839 ± 0.128	$7.375/16$
		60–70%	0.178 ± 0.004	0.62 ± 0.11	0.342 ± 0.015	1.411 ± 0.062	$2.427/16$
Figure 5f	\bar{p}	0–5%	0.237 ± 0.004	0.88 ± 0.08	0.270 ± 0.054	8.086 ± 0.380	$9.659/17$
		5–10%	0.231 ± 0.004	0.85 ± 0.11	0.310 ± 0.062	6.970 ± 0.293	$9.818/17$
		10–20%	0.228 ± 0.005	0.82 ± 0.12	0.306 ± 0.060	5.318 ± 0.261	$6.490/17$
		20–30%	0.218 ± 0.004	0.86 ± 0.10	0.255 ± 0.051	3.722 ± 0.164	$8.283/17$
		30–40%	0.213 ± 0.004	0.83 ± 0.13	0.274 ± 0.054	2.756 ± 0.168	$0.376/17$
		40–50%	0.204 ± 0.004	0.74 ± 0.14	0.325 ± 0.029	1.824 ± 0.071	$3.573/17$
		50–60%	0.189 ± 0.003	0.72 ± 0.14	0.311 ± 0.013	1.152 ± 0.045	$3.976/17$
		60–70%	0.182 ± 0.003	0.75 ± 0.15	0.296 ± 0.013	0.636 ± 0.028	$10.249/17$
		70–80%	0.172 ± 0.003	0.71 ± 0.14	0.281 ± 0.014	0.335 ± 0.014	$23.783/17$

Table 6. Values of free parameters, normalization constant, and χ^2/dof corresponding to the two-component Erlang p_T distribution for production in Au-Au collisions at $\sqrt{s_{NN}} = 62.4\text{ GeV}$ for different centralities in Figure 6. (m_1 equals 2, 3, and 4 for π^\pm , K^\pm , and $p(\bar{p})$, respectively; m_2 equals 2 for all particles.)

Figure	Particle	Centrality	$\langle p_{t1} \rangle$ (GeV/c)	k_1	$\langle p_{t2} \rangle$ (GeV/c)	N_0	χ^2/dof
Figure 6a	π^+	0–5%	0.172 ± 0.003	0.65 ± 0.05	0.274 ± 0.012	232.461 ± 1.860	$0.261/4$
		5–10%	0.188 ± 0.003	0.85 ± 0.04	0.314 ± 0.022	187.816 ± 1.315	$0.361/4$
		10–20%	0.156 ± 0.003	0.51 ± 0.03	0.261 ± 0.009	146.014 ± 1.168	$0.344/4$
		20–30%	0.158 ± 0.002	0.51 ± 0.03	0.257 ± 0.008	99.959 ± 0.800	$0.468/4$
		30–40%	0.153 ± 0.003	0.51 ± 0.03	0.256 ± 0.009	67.869 ± 0.611	$0.406/4$
		40–50%	0.147 ± 0.002	0.51 ± 0.03	0.254 ± 0.008	44.560 ± 0.356	$0.563/4$
		50–60%	0.145 ± 0.002	0.51 ± 0.02	0.245 ± 0.008	27.279 ± 0.164	$1.851/4$
		60–70%	0.141 ± 0.002	0.53 ± 0.02	0.241 ± 0.011	15.409 ± 0.092	$0.508/4$
		70–80%	0.136 ± 0.002	0.51 ± 0.02	0.230 ± 0.008	7.645 ± 0.054	$1.175/4$
Figure 6d	π^-	0–5%	0.175 ± 0.002	0.67 ± 0.05	0.269 ± 0.008	234.954 ± 1.410	$0.825/4$
		5–10%	0.175 ± 0.003	0.73 ± 0.05	0.298 ± 0.026	193.787 ± 2.519	$1.483/4$
		10–20%	0.161 ± 0.003	0.56 ± 0.04	0.267 ± 0.009	147.565 ± 1.328	$0.072/4$
		20–30%	0.164 ± 0.003	0.59 ± 0.04	0.265 ± 0.011	101.980 ± 0.918	$0.091/4$
		30–40%	0.159 ± 0.003	0.58 ± 0.04	0.269 ± 0.012	68.737 ± 0.619	$0.120/4$
		40–50%	0.148 ± 0.002	0.51 ± 0.04	0.257 ± 0.007	44.980 ± 0.270	$0.867/4$
		50–60%	0.160 ± 0.002	0.69 ± 0.06	0.297 ± 0.018	27.748 ± 0.361	$0.148/4$
		60–70%	0.157 ± 0.002	0.71 ± 0.04	0.303 ± 0.021	15.342 ± 0.199	$0.412/4$
		70–80%	0.138 ± 0.002	0.51 ± 0.02	0.228 ± 0.008	7.692 ± 0.046	$0.572/4$
Figure 6b	K^+	0–5%	0.246 ± 0.004	0.75 ± 0.04	0.256 ± 0.015	39.598 ± 0.752	$0.299/4$
		5–10%	0.236 ± 0.004	0.63 ± 0.10	0.310 ± 0.010	32.688 ± 0.490	$1.425/4$
		10–20%	0.248 ± 0.003	0.69 ± 0.06	0.269 ± 0.009	24.648 ± 0.320	$1.034/4$
		20–30%	0.226 ± 0.008	0.57 ± 0.11	0.302 ± 0.020	15.892 ± 0.445	$5.988/4$
		30–40%	0.247 ± 0.008	0.57 ± 0.10	0.252 ± 0.019	11.179 ± 0.291	$0.500/4$
		40–50%	0.224 ± 0.005	0.51 ± 0.11	0.266 ± 0.013	7.046 ± 0.127	$2.632/4$
		50–60%	0.234 ± 0.006	0.51 ± 0.07	0.275 ± 0.010	4.065 ± 0.081	$0.345/4$
		60–70%	0.217 ± 0.005	0.62 ± 0.12	0.231 ± 0.013	2.147 ± 0.045	$3.387/4$
		70–80%	0.213 ± 0.011	0.51 ± 0.12	0.233 ± 0.020	0.934 ± 0.031	$5.179/4$
Figure 6e	K^-	0–5%	0.235 ± 0.021	0.81 ± 0.14	0.281 ± 0.057	33.071 ± 1.885	$7.217/4$
		5–10%	0.226 ± 0.004	0.73 ± 0.14	0.288 ± 0.017	26.889 ± 0.511	$3.348/4$
		10–20%	0.228 ± 0.003	0.72 ± 0.12	0.291 ± 0.010	20.235 ± 0.243	$3.616/4$
		20–30%	0.222 ± 0.003	0.71 ± 0.14	0.292 ± 0.010	14.319 ± 0.172	$3.191/4$
		30–40%	0.218 ± 0.004	0.71 ± 0.09	0.279 ± 0.015	9.119 ± 0.173	$2.298/4$
		40–50%	0.208 ± 0.003	0.71 ± 0.14	0.265 ± 0.010	5.810 ± 0.070	$5.979/4$
		50–60%	0.195 ± 0.004	0.66 ± 0.13	0.282 ± 0.017	3.421 ± 0.072	$4.352/4$
		60–70%	0.187 ± 0.003	0.71 ± 0.14	0.261 ± 0.012	1.777 ± 0.023	$5.638/4$
		70–80%	0.178 ± 0.012	0.78 ± 0.16	0.194 ± 0.040	0.788 ± 0.037	$8.929/4$
Figure 6c	p	0–5%	0.256 ± 0.002	0.92 ± 0.04	0.336 ± 0.031	28.857 ± 0.231	$4.730/9$
		5–10%	0.253 ± 0.001	0.91 ± 0.03	0.382 ± 0.016	23.302 ± 0.140	$7.145/9$
		10–20%	0.247 ± 0.001	0.93 ± 0.04	0.347 ± 0.027	17.611 ± 0.123	$6.489/9$
		20–30%	0.237 ± 0.002	0.96 ± 0.02	0.315 ± 0.045	11.620 ± 0.116	$20.228/9$
		30–40%	0.229 ± 0.001	0.98 ± 0.02	0.273 ± 0.038	7.729 ± 0.046	$6.932/9$
		40–50%	0.221 ± 0.001	0.96 ± 0.04	0.330 ± 0.022	4.845 ± 0.029	$6.636/9$
		50–60%	0.209 ± 0.001	0.95 ± 0.05	0.380 ± 0.029	2.854 ± 0.017	$13.302/9$
		60–70%	0.197 ± 0.002	0.97 ± 0.03	0.360 ± 0.047	1.465 ± 0.010	$13.381/9$
		70–80%	0.188 ± 0.002	0.95 ± 0.04	0.207 ± 0.043	0.647 ± 0.006	$20.066/9$
Figure 6f	\bar{p}	0–5%	0.289 ± 0.002	0.77 ± 0.01	0.395 ± 0.007	15.211 ± 0.122	$10.907/10$
		5–10%	0.285 ± 0.002	0.80 ± 0.03	0.346 ± 0.011	12.675 ± 0.139	$9.012/10$
		10–20%	0.269 ± 0.002	0.84 ± 0.01	0.312 ± 0.013	9.551 ± 0.105	$13.318/10$
		20–30%	0.255 ± 0.002	0.82 ± 0.02	0.312 ± 0.018	6.532 ± 0.046	$13.768/10$
		30–40%	0.240 ± 0.002	0.77 ± 0.04	0.349 ± 0.013	4.335 ± 0.030	$12.088/10$
		40–50%	0.227 ± 0.002	0.81 ± 0.02	0.264 ± 0.020	2.811 ± 0.034	$5.505/10$
		50–60%	0.208 ± 0.002	0.79 ± 0.05	0.307 ± 0.011	1.688 ± 0.014	$6.896/10$
		60–70%	0.201 ± 0.002	0.67 ± 0.05	0.317 ± 0.021	0.963 ± 0.009	$8.320/10$
		70–80%	0.179 ± 0.003	0.67 ± 0.06	0.318 ± 0.034	0.433 ± 0.005	$21.387/10$

According to the extracted normalization constants from the above comparisons, the yield ratios of negative to positive particles, k_π , k_K , and k_p , versus collision energy and centrality are obtained. The three types of yield ratios show regular trends with an increase in collision energy and centrality. In order to see the dependencies of the three yield ratios on centrality, Figures 7–9, respectively, show the change trends of the three yield ratios of k_π , k_K , and k_p with different centralities at different energies. As can be seen, k_π varies by approximately 1.05 and decreases with increase in energy, but does not show a visible dependence on centrality. k_K varies between 0.35 and 0.85, and increases obviously with increase of energy. At some energies (7.7, 11.5, 19.6 and 39 GeV), k_K increases with increase in centrality class, but at these energies of 27 and 62.4 GeV, k_K do not show an evident dependence on centrality. k_p varies between 0.007 and 0.7, and prominently increases with the increase in energy. Unlike k_π and k_K , k_p obviously increases with increase in centrality class at all energies, which means that k_p shows an obvious dependence on centrality. Overall, the dependence of k_p on centrality is higher than that of k_K , and the dependence of k_K on centrality is higher than that of k_π , which indicates that the correlation between the generation mechanism of p (\bar{p}) and centrality is relatively the highest, followed by K^\pm , and π^\pm is the weakest. In addition, it is not difficult to notice that with the increase in energy, the values of k_K and k_p are both less than 1 and gradually increase (most cases), while that of k_π are almost equal to 1, which indicates that the generation mechanisms of these particles are closely related to the collision energy, and the generation mechanism of p and \bar{p} is similar to K^\pm , but different from π^\pm .

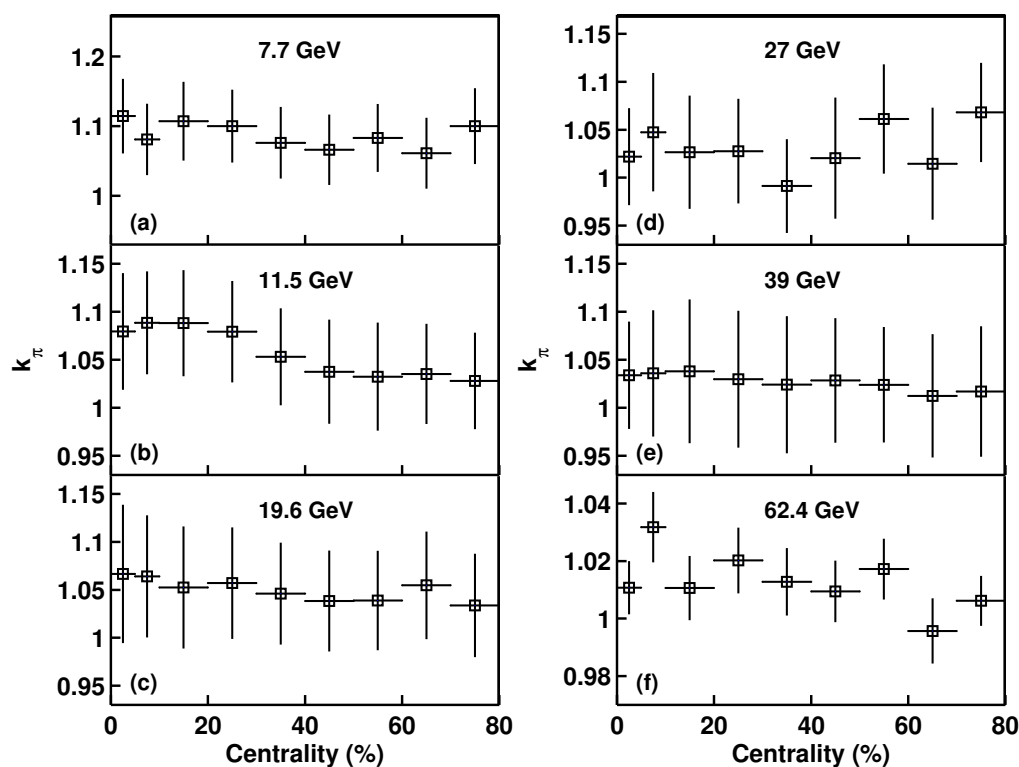


Figure 7. Centrality-dependent k_π at different energies of (a) 7.7; (b) 11.5; (c) 19.6; (d) 27; (e) 39; and (f) 62.4 GeV.

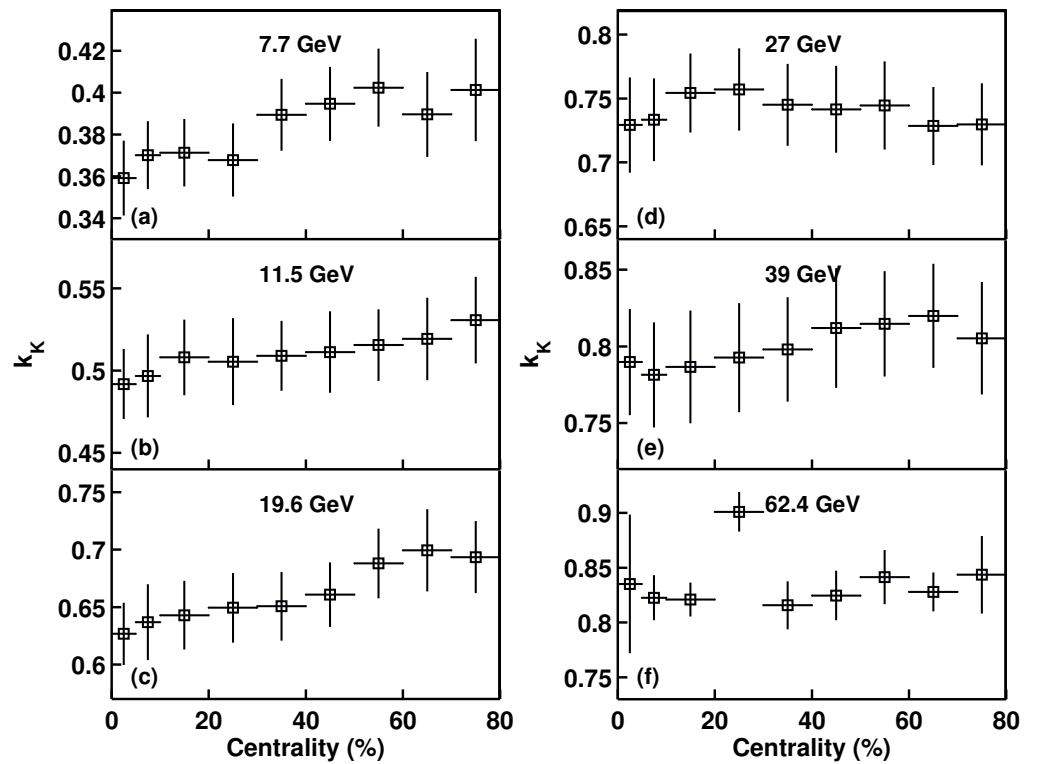


Figure 8. Same as Figure 7 for k_K .

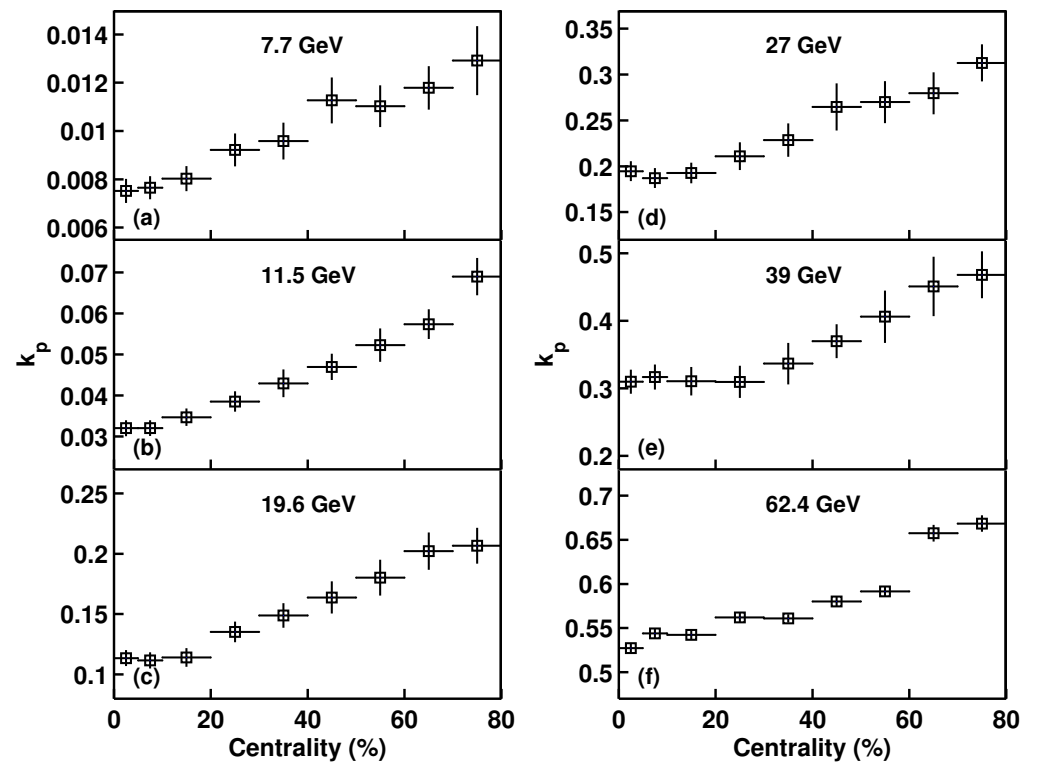


Figure 9. Same as Figure 7 for k_p .

In Figures 7–9, one can see that the three types of yield ratios obviously depend on the collision energy, and we find that the logarithms of the three types of yield ratios, $\ln(k_\pi)$,

$\ln(k_K)$, and $\ln(k_p)$, show a distinct linear dependence on $1/\sqrt{s_{NN}}$, a linear relationship which can be expressed as

$$\ln(k_{ij}) = A_{ij}/\sqrt{s_{NN}} + B_{ij}, \quad (11)$$

where i represents π , K , or p , j represent different centrality classes, and A_{ij} and B_{ij} are fitting parameters. Figure 10 shows the $1/\sqrt{s_{NN}}$ -dependent (a) $\ln(k_\pi)$, (b) $\ln(k_K)$, and (c) $\ln(k_p)$ for different centralities. The fitting lines are the results calculated by the least squares method. The values of calculated parameters (A_{ij} and B_{ij}) and χ^2/dof are listed in Table 7. It is not hard to see that, the values of intercept B_{ij} are asymptotically zero, which means the limiting values of the yield ratios are one at very high energy. For the same particle, the slope A_{ij} does not change much with the increase in centrality, especially for π . To see clearly the dependences of the linear relationships on centrality, the results for different centrality classes are added by appropriate factors shown in different panels of Figure 10.

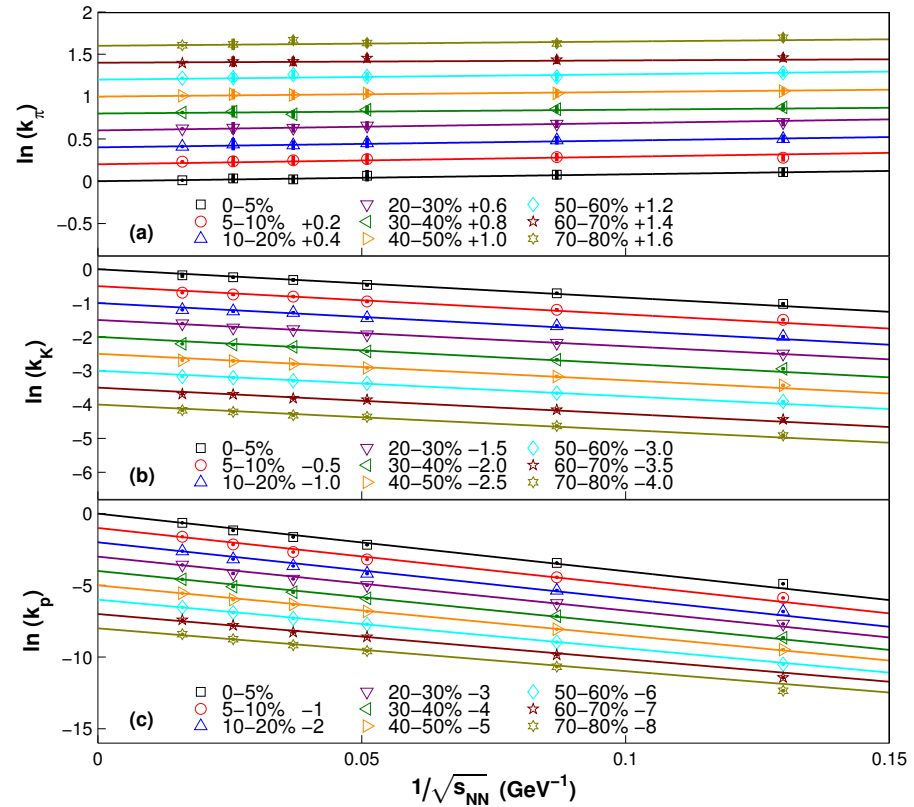


Figure 10. Energy-dependent (a) $\ln(k_\pi)$, (b) $\ln(k_K)$, and (c) $\ln(k_p)$ for different centralities. The fitting lines are the results calculated by least squares method. For clarity, the results for different centralities are added by appropriate factors shown in different panels.

As can be seen, with the increase in $\sqrt{s_{NN}}$, $\ln(k_K)$ and $\ln(k_p)$ increase, while $\ln(k_\pi)$ decreases, which implies that the generation mechanism of K is similar to p , but is different from π . The differences of the cross-section of absorption, the content of primary proton in nuclei and so on can result in the differences of the yields of these particles. From Table 7, one can see that the centrality-dependent A_π varies roughly between 0.48 and 0.89, and does not show an obvious change trend with centrality. A_K and A_p vary roughly from -7.52 to -6.63 and from -38.86 to -33.42 , respectively, and an overall decrease with centrality, and the increase in A_p is relatively prominent. These indicate that although the dependence of the energy-dependent yield ratio of p on centrality is higher than that of

K , and that of K is higher than that of π , the dependencies of the three energy-dependent yield ratios on centrality are not evident.

Table 7. Values of free parameters and χ^2/dof corresponding to the fitting lines in Figure 10.

Figure	Particle	Centrality	A_{ij}	B_{ij}	χ^2/dof
Figure 10a	π	0–5%	0.886 ± 0.399	-0.003 ± 0.010	0.209/3
		5–10%	0.507 ± 0.376	0.024 ± 0.013	0.229/3
		10–20%	0.880 ± 0.459	-0.003 ± 0.012	0.171/3
		20–30%	0.703 ± 0.403	0.009 ± 0.012	0.086/3
		30–40%	0.544 ± 0.370	0.003 ± 0.013	0.516/3
		40–50%	0.482 ± 0.370	0.002 ± 0.011	0.114/3
		50–60%	0.500 ± 0.379	0.010 ± 0.012	0.511/3
		60–70%	0.613 ± 0.426	-0.013 ± 0.013	0.507/3
Figure 10b	K	0–5%	-7.522 ± 0.444	-0.055 ± 0.032	0.656/3
		5–10%	-7.086 ± 0.349	-0.075 ± 0.028	0.622/3
		10–20%	-6.956 ± 0.424	-0.076 ± 0.030	2.076/3
		20–30%	-7.922 ± 0.501	0.011 ± 0.036	1.985/3
		30–40%	-6.667 ± 0.313	-0.081 ± 0.027	1.503/3
		40–50%	-6.641 ± 0.324	-0.073 ± 0.026	1.162/3
		50–60%	-6.688 ± 0.323	-0.053 ± 0.023	1.122/3
		60–70%	-6.637 ± 0.499	-0.068 ± 0.040	2.414/3
Figure 10c	p	0–5%	-38.697 ± 1.583	-0.031 ± 0.138	32.951/3
		5–10%	-38.855 ± 3.000	-0.002 ± 0.200	46.465/3
		10–20%	-38.147 ± 1.051	-0.014 ± 0.092	37.401/3
		20–30%	-37.168 ± 0.600	0.010 ± 0.029	23.505/3
		30–40%	-36.214 ± 0.725	-0.001 ± 0.012	7.260/3
		40–50%	-35.067 ± 0.523	0.014 ± 0.014	3.675/3
		50–60%	-34.785 ± 0.479	0.032 ± 0.010	1.071/3
		60–70%	-35.004 ± 0.530	0.140 ± 0.016	3.368/3
		70–80%	-33.417 ± 0.978	0.131 ± 0.016	4.916/3

Based on the extracted yield ratios and Equations (9) and (10), the energy- and centrality-dependent light hadron chemical potentials, μ_π , μ_K , and μ_p , of π , K , and p , and quark chemical potentials, μ_u , μ_d , and μ_s , of u , d , and s quarks, respectively, were obtained and are shown in Figure 11. The different symbols denote the calculated results of different centrality classes. The curves are the derivative results according to Equation (11) corresponding to the fitted lines in Figure 10. As can be seen, in the energy range from 7.7 to 62.4 GeV, μ_π increases, and μ_K , μ_p , μ_u , μ_d , and μ_s obviously decrease with the increase in $\sqrt{s_{NN}}$. From the trends of the curves, the limiting values of the six types of chemical potentials are asymptotically zero at very high energy. The differences between chemical potentials of particles with different centralities are relatively large in the low energy region, and as the energy increases the differences gradually decrease, and finally tend to be zero at very high energy. These results are consistent with the results obtained in the references [41–43]. μ_p obtained in this work is smaller than μ_B in reference [43]. For an energy range from 7.7 to 39 GeV, the relative difference is mainly within 10%. However, the relative difference increases to approximately 20% at 62.4 GeV. In addition, at the same energy, μ_K is larger than $|\mu_\pi|$ but less than μ_p , and μ_u is almost as large as μ_d but larger than μ_s due to the differences in the different particle masses.

It is not hard to notice that $\mu_\pi < 0$, while $\mu_K(\mu_p, \mu_u, \mu_d, \mu_s) > 0$. This is caused by $k_\pi > 1$, while $k_K(k_p) < 1$. When the energy increases to a very high value, all chemical potentials of light hadrons and quarks approach zero, when the partonic interactions possibly play a dominant role, the mean-free-path of particles becomes large, and the collision system possibly changes completely from the hadron-dominant state to the quark-dominant state.

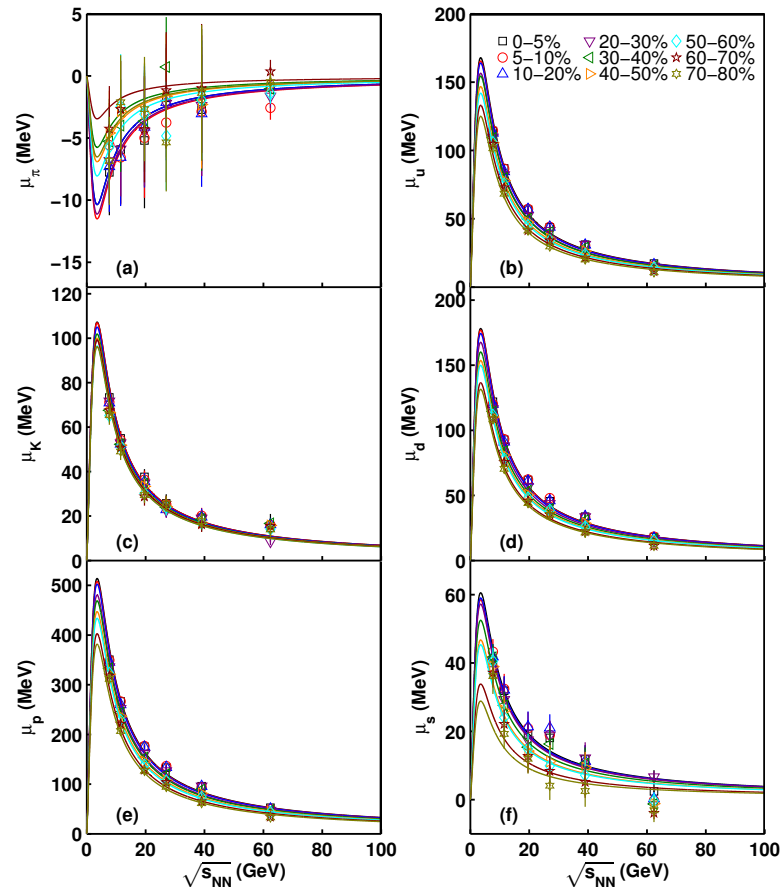


Figure 11. Dependencies of centrality-dependent hadron chemical potentials: (a) μ_π ; (b) μ_K ; and (c) μ_p and quark chemical potentials; (d) μ_u ; (e) μ_d ; and (f) μ_s , on energy $\sqrt{s_{NN}}$. The different symbols denote the calculated results in different centrality classes according to the extracted yield ratios and Equations (9) and (10), and the curves are the derivative results based on the linear fits in Figure 10.

In Figure 11, as in our previous work [21], the derived curves of particle chemical potentials from the linear fits of the energy-dependent yield ratios in Figure 10 simultaneously show the maximum (the absolute magnitude for π) at 3.526 GeV, which is not observed from the linear fits. The energy at the maximum can be obtained according to the calculation method in reference [21]. According to Equations (7) and (9)–(11), we can obtain the chemical potentials (μ_{kj}) of hadrons and quarks for all centrality classes in terms of $\sqrt{s_{NN}}$. Considering that all the values of intercept B_{ij} in Table 7 are approximately zero and the simplicity for calculation, we set $B_{ij} = 0$ here, and the μ_{kj} can be written as

$$\mu_{kj} = T_{ch} \frac{C_{kj}}{\sqrt{s_{NN}}}, \quad (12)$$

where $k = \pi, K, p, u, d$, and s, j represents different centralities, and C_{kj} is a linear combination of A_{ij} , i.e.,

$$\begin{cases} C_{\pi j} = -\frac{1}{2}A_{\pi j}, \\ C_{K j} = -\frac{1}{2}A_{K j}, \\ C_{p j} = -\frac{1}{2}A_{p j}, \\ C_{u j} = -\frac{1}{6}(A_{\pi j} + A_{p j}), \\ C_{d j} = -\frac{1}{6}(-2A_{\pi j} + A_{p j}), \\ C_{s j} = -\frac{1}{6}(A_{\pi j} - 2A_{K j} + A_{p j}). \end{cases} \tag{13}$$

Let $\frac{d\mu_{ij}}{d\sqrt{s_{NN}}} = 0$, and we obtain the energy value ($\sqrt{s_{NN}} = 3.526$ GeV) at the maximum.

It must be emphasized that, due to the lack of data in a low-energy region, the maximum here is only a prediction according to these linear fits, not a certainty. The energy 3.526 GeV at the maximum possibly is the critical energy of phase transition from a liquid-like hadron state to a gas-like quark state in the collision system. At this special energy, the chemical potentials for all cases have the maximum, which indicates that the density of the baryon number has the largest value and the mean-free-path of particles has the smallest value. This means that the hadronic interactions play an important role at this special stage. When the energy is higher than 3.526 GeV, these chemical potentials gradually decrease with the increase of energy, which indicates that the density of baryon number gradually decreases [9], the mean-free-path increases, the shear viscosity over entropy density gradually weakens [44], the hadronic interactions gradually fade, and the partonic interactions gradually become greater. When the energy increases to a very high value, especially the LHC energy, the chemical potentials of all types of particles approach zero, which means that the density of the baryon number and the viscous effect approach zero, and the collision system possibly changes completely from the hadron-dominant state to the quark-dominant state, which denotes the partonic interactions possibly play a dominant role at very high energy [1,45], and the strongly coupled QGP (sQGP) has been observed [5–7].

We must point out that, since the maximum is predicted by the empirical formula, the critical energy value extracted from it has a large fluctuation. In other words, although the fluctuation exists or is even large, it does not mean that the extracted energy value must be wrong. Thus, at the extracted energy, there may be a phase transition critical point. The extracted critical energy (3.526 GeV) of phase transition is consistent with our previous result [21] and the result (below 19.6 GeV) by the STAR Collaboration [1], but less than the result (between 11.5 GeV and 19.6 GeV) of a study based on a correlation between the collision energy and transverse momentum [39,45,46]. Therefore, we still need to make more efforts to find or correct the critical energy point through new methods or theories.

4. Summary and Conclusions

The p_T spectra of final-state light flavor particles, π^\pm , K^\pm , p , and \bar{p} , produced in Au-Au collisions for different centralities over an energy range from 7.7 to 62.4 GeV are described by a two-component Erlang distribution in the frame of a multi-source thermal model. The fitting results are in agreement with the experimental data recorded by the STAR Collaboration.

The fitting parameters of two-component Erlang p_T distribution shows that, the first component corresponding to a narrow low- p_T region is contributed by the soft excitation process where a few (2–4) sea quarks and gluons take part in, and the second component corresponding to a wide high- p_T region is contributed by the hard scattering process coming from a more violent collision between two valence quarks in incident nucleons. The relative weight factor of a soft excitation process shows that the contribution ratio of

a soft excitation process is more than 60%, which indicates that the excitation degree of collision system is mainly contributed by the soft excitation process.

The yield ratios, k_π , k_K , and k_p , of negative to positive particle versus collision energy, and centrality are obtained from the normalization constants. This study shows that, although the dependence of k_p on centrality is higher than that of k_K , the dependence of k_K on centrality is higher than that of k_π , the dependences of the three yield ratios on centrality are not significant, especially for π . The logarithms of the three types of yield ratios, $\ln(k_\pi)$, $\ln(k_K)$, and $\ln(k_p)$, show obvious linear dependence on $1/\sqrt{s_{NN}}$.

The energy- and centrality-dependent chemical potentials of light hadrons, μ_π , μ_K , and μ_p , and quarks, μ_u , μ_d , and μ_s , are extracted from the yield ratios. With the increase in energy over a range from 7.7 to 62.4 GeV, all the chemical potentials (the absolute magnitude for π) obviously decrease. When the collision energy is very high, all types of chemical potentials are small and tend to be a limiting value of zero. Overall, the dependencies of the six types of energy-dependent chemical potentials on centrality are relatively more obvious in the low energy region than that in the high energy region, but the six energy-dependent chemical potentials in different centrality classes are very close, which indicates that the dependencies of the energy-dependent chemical potentials from Au-Au collisions on centrality are relatively not so significant.

All the derived curves of energy- and centrality-dependent chemical potentials of hadrons and quarks, based on the linear relationships between the logarithms of yield ratios and $1/\sqrt{s_{NN}}$, simultaneously show the maximum (the absolute magnitude for π) at 3.526 GeV, which is possibly the critical energy of phase transition from a liquid-like hadron state to a gas-like quark state in the collision system, when the density of the baryon number in Au-Au collisions has a large value and the hadronic interactions play an important role. When energy continues to increase, all types of chemical potentials become small, which indicates the density of a baryon number gradually decreases, the mean-free-path gradually increases, and the viscous effect gradually weakens. At this time, the hadronic interactions gradually fade and the partonic interactions gradually become greater. When the energy rises to a very high value, especially to the LHC, all types of chemical potentials tend towards zero, which indicates that the collision system possibly completely changes from the liquid-like hadron-dominant state to the gas-like quark-dominant state when the partonic interactions possibly play a dominant role.

Author Contributions: Conceptualization, H.-R.W.; methodology, B.-H.H.; software, H.-Y.W.; validation, X.-W.H. and H.-R.W.; formal analysis, H.-R.W.; investigation, X.-W.H. and H.-R.W.; resources, H.-R.W.; data curation, X.-W.H.; writing—original draft preparation, H.-R.W.; writing—review and editing, W.-T.Z.; visualization, X.-W.H.; supervision, F.-M.W.; project administration, F.-M.W.; funding acquisition, H.-R.W. All authors have read and agreed to the published version of the manuscript.

Funding: This work was supported by the National Natural Science Foundation of China under Grant Nos. 11847114.

Institutional Review Board Statement: Not applicable.

Informed Consent Statement: Not applicable.

Data Availability Statement: All data are quoted from the mentioned references. As a phenomenological work, this paper does not report new data.

Conflicts of Interest: The authors declare that there are no conflicts of interest regarding the publication of this paper.

References

1. Xu, N. [STAR Collaboration]. An overview of STAR experimental results. *Nucl. Phys. A* **2014**, *931*, 1–12. [[CrossRef](#)]
2. Cleymans, J.; Oeschler, H.; Redlich, H.; Wheaton, S. Comparison of chemical freeze-out criteria in heavy-ion collisions. *Phys. Rev. C* **2006**, *73*, 034905. [[CrossRef](#)]
3. Rischke, D.H. The quark–gluon plasma in equilibrium. *Prog. Part. Nucl. Phys.* **2004**, *52*, 197–296. [[CrossRef](#)]
4. Cabibbo, N.; Parisi, G. Exponential hadronic spectrum and quark liberation. *Phys. Lett. B* **1975**, *59*, 67–69. [[CrossRef](#)]

5. Bazavov, A.; et al. [Fermilab Lattice and MILC Collaborations]. B - and D -meson decay constants from three-flavor lattice QCD. *Phys. Rev. D* **2012**, *85*, 114506. [[CrossRef](#)]
6. Adams, J.; et al. [STAR Collaboration]. Experimental and theoretical challenges in the search for the quark–gluon plasma: The STAR Collaboration’s critical assessment of the evidence from RHIC collisions. *Nucl. Phys. A* **2005**, *757*, 102–183. [[CrossRef](#)]
7. Grosse-Oetringhaus, J.F. [ALICE Collaboration]. Overview of ALICE results at Quark Matter 2014. *Nucl. Phys. A* **2014**, *931*, 22–31. [[CrossRef](#)]
8. Braun-Munzinger, P.; Wambach, J. *Colloquium*: Phase diagram of strongly interacting matter. *Rev. Mod. Phys.* **2009**, *81*, 1031. [[CrossRef](#)]
9. Braun-Munzinger, P.; Stachel, J. The quest for the quark–gluon plasma. *Nature* **2007**, *448*, 302–309. [[CrossRef](#)]
10. Stephanov, M.A. QCD phase diagram: An overview. *arXiv* **2006**, arXiv:hep-lat/0701002
11. Wygas, M.M.; Oldengott, I.M.; Bödeker, D.; Schwarz, D.J. Cosmic QCD epoch at nonvanishing lepton asymmetry. *Phys. Rev. Lett.* **2018**, *121*, 201302. [[CrossRef](#)] [[PubMed](#)]
12. Domdey, S.; Kopeliovich, B.Z.; Pirner, H.J. Jet-evolution in the quark-gluon plasma from RHIC to the LHC. *Nucl. Phys. A* **2011**, *856*, 134–153. [[CrossRef](#)]
13. Liu, F.H.; Chen, J.Y.; Zhang, Q. Multisource thermal model describing transverse momentum spectra of final-state particles in high-energy collisions. *Adv. High Energy Phys.* **2022**, *2022*, 7274958. [[CrossRef](#)]
14. Zhang, X.H.; Gao, Y.Q.; Liu, F.H.; Olimov, K.K. Thermal freeze-Out parameters and pseudoentropy from charged hadron spectra in high-energy collisions. *Adv. High Energy Phys.* **2022**, *2022*, 7499093. [[CrossRef](#)]
15. Zhang, Q.; Gao, Y.Q.; Liu, F.H.; Olimov, K.K. An energy independent scaling of transverse momentum spectra of direct (prompt) photons from two-body processes in high-energy proton–proton collisions. *Ann. Phys.* **2021**, *534*, 2100567. [[CrossRef](#)]
16. Gupta, N. A Study of Fluctuations in Multiplicity Distributions at Ultra-Relativistic Heavy Ion Interactions. Ph.D. Thesis, University of Jammu, Jammu, India, 2008.
17. Wei, H.R.; Liu, F.H.; Lacey, R.A. Kinetic freeze-out temperature and flow velocity extracted from transverse momentum spectra of final-state light flavor particles produced in collisions at RHIC and LHC. *Eur. Phys. J. A* **2016**, *52*, 102. [[CrossRef](#)]
18. Zhao, H.; Liu, F.H. Chemical potentials of quarks extracted from particle transverse momentum distributions in heavy ion collisions at RHIC energies. *Adv. High Energy Phys.* **2014**, *2014*, 742193. [[CrossRef](#)]
19. Zhao, H.; Liu, F.H. On extraction of chemical potentials of quarks from particle transverse momentum spectra in high energy collisions. *Adv. High Energy Phys.* **2015**, *2015*, 137058. [[CrossRef](#)]
20. He, X.W.; Wei, H.R.; Liu, F.H. Chemical potentials of light hadrons and quarks from yield ratios of negative to positive particles in high energy pp collisions. *J. Phys. G Nucl. Part. Phys.* **2019**, *46*, 025102. [[CrossRef](#)]
21. He, X.W.; Wu, F.M.; Wei, H.R.; Hong, B.H. Energy-dependent chemical potentials of light hadrons and quarks based on transverse momentum spectra and yield ratios of negative to positive particles. *Adv. High Energy Phys.* **2020**, *2020*, 1265090. [[CrossRef](#)]
22. Wei, H.R.; Liu, F.H.; Lacey, R.A. Disentangling random thermal motion of particles and collective expansion of source from transverse momentum spectra in high energy collisions. *J. Phys. G Nucl. Part. Phys.* **2016**, *43*, 125102. [[CrossRef](#)]
23. Siemens, P.J.; Rasmussen, J.O. Evidence for a blast wave from compressed nuclear matter. *Phys. Rev. Lett.* **1979**, *42*, 880. [[CrossRef](#)]
24. Zhang, H. [STAR Collaboration]. Open charm production at STAR. *J. Phys. G Nucl. Part. Phys.* **2004**, *31*, S267. [[CrossRef](#)]
25. Wilk, G.; Włodarczyk, Z. Interpretation of the nonextensivity parameter q in some applications of Tsallis statistics and Lévy distributions. *Phys. Rev. Lett.* **2000**, *84*, 2770. [[CrossRef](#)] [[PubMed](#)]
26. Liu, F.H.; Li, J.S. Isotopic production cross section of fragments in $^{56}\text{Fe} + p$ and $^{136}\text{Xe}(^{124}\text{Xe}) + \text{Pb}$ reactions over an energy range from 300A to 1500A MeV. *Phys. Rev. C* **2008**, *78*, 044602. [[CrossRef](#)]
27. Liu, F.H. Unified description of multiplicity distributions of final-state particles produced in collisions at high energies. *Nucl. Phys. A* **2008**, *810*, 159–172. [[CrossRef](#)]
28. Liu, F.H.; Abd Allah, N.N.; Singh B.K. Dependence of black fragment azimuthal and projected angular distributions on polar angle in silicon-emulsion collisions at 4.5A GeV/c. *Phys. Rev. C* **2004**, *69*, 057601. [[CrossRef](#)]
29. Liu, F.H. Dependence of charged particle pseudorapidity distributions on centrality and energy in $p(d)A$ collisions at high energies. *Phys. Rev. C* **2008**, *78*, 014902. [[CrossRef](#)]
30. Dumitru, A.; Portugal, L.; Zschieche, D. Inhomogeneous freeze-out in relativistic heavy-ion collisions. *Phys. Rev. C* **2006**, *73*, 024902. [[CrossRef](#)]
31. Yu, N.; Luo X.F. Particle decay from statistical thermal model in high-energy nucleus-nucleus collisions. *Eur. Phys. J. A* **2019**, *55*, 26. [[CrossRef](#)]
32. Lao, H.L.; Gao, Y.Q.; Liu F.H. Light particle and quark chemical potentials from negatively to positively charged particle yield ratios corrected by removing strong and weak decays. *Adv. High Energy Phys.* **2020**, *2020*, 5064737. [[CrossRef](#)]
33. Adamczyk, L.; et al. [STAR Collaboration]. Bulk properties of the medium produced in relativistic heavy-ion collisions from the beam energy scan program. *Phys. Rev. C* **2017**, *96*, 044904. [[CrossRef](#)]
34. Abelev B.I.; et al. [STAR Collaboration]. Systematic measurements of identified particle spectra in pp , $d+Au$, and Au–Au collisions at the STAR detector. *Phys. Rev. C* **2009**, *79*, 034909. [[CrossRef](#)]
35. Braun-Munzinger, P.; Magestro, D.; Redlich, K.; Stachel, J. Hadron production in Au–Au collisions at RHIC. *Phys. Lett. B* **2001**, *518*, 41–46. [[CrossRef](#)]

36. Adler, S.S.; et al. [PHENIX Collaboration]. Identified charged particle spectra and yields in Au-Au collisions at $\sqrt{s_{NN}}=200$ GeV. *Phys. Rev. C* **2004**, *69*, 034909. [[CrossRef](#)]
37. Andronic, A.; Braun-Munzinger, P.; Stachel, J. Thermal hadron production in relativistic nuclear collisions. *Acta Phys. Pol. B* **2009**, *40*, 1005–1012.
38. Kovács, P.; Szép, Z. Influence of the isospin and hypercharge chemical potentials on the location of the critical end point in the μ_B - T phase diagram of the $SU(3)_L \times SU(3)_R$ chiral quark model. *Phys. Rev. D* **2008**, *77*, 065016. [[CrossRef](#)]
39. Abelev, B.; et al. [ALICE Collaboration]. $K^*(892)^0$ and $\phi(1020)$ production in Pb-Pb collisions at $\sqrt{s_{NN}}=2.76$ TeV. *Phys. Rev. C* **2015**, *91*, 024609. [[CrossRef](#)]
40. Arsene, I.; et al. [BRAHMS Collaboration]. Quark–gluon plasma and color glass condensate at RHIC? The perspective from the BRAHMS experiment. *Nucl. Phys. A* **2005**, *757*, 1–27. [[CrossRef](#)]
41. Bhattacharyya, S.; Biswas, D.; Ghosh, S.K.; Ray, R.; Singha, P. Novel scheme for parametrizing the chemical freeze-out surface in heavy ion collision experiments. *Phys. Rev. D* **2019**, *100*, 054037. [[CrossRef](#)]
42. Bhattacharyya, S.; Biswas, D.; Ghosh, S.K.; Ray, R.; Singha, P. Systematics of chemical freeze-out parameters in heavy-ion collision experiments. *Phys. Rev. D* **2020**, *101*, 054002. [[CrossRef](#)]
43. Biswas, D. Centrality dependence of chemical freeze-out parameters and strangeness equilibration in RHIC and LHC energies. *Adv. High Energy Phys.* **2021**, *2021*, 6611394. [[CrossRef](#)]
44. Gyulassy, M.; McLerran, L. New forms of QCD matter discovered at RHIC. *Nucl. Phys. A* **2005**, *750*, 30–63. [[CrossRef](#)]
45. Abelev, B.I.; et al. [STAR Collaboration]. Measurements of ϕ meson production in relativistic heavy-ion collisions at the BNL Relativistic Heavy Ion Collider (RHIC). *Phys. Rev. C* **2009**, *79*, 064903. [[CrossRef](#)]
46. Nasim, M.; Bairathi, V.; Sharma, M.K.; Mohanty, B.; Bhasin, A. A review on ϕ meson production in heavy-ion collision. *Adv. High Energy Phys.* **2015**, *2015*, 197930.